

Scalable Temporal Anomaly Causality Discovery in Large Systems: Achieving Computational Efficiency with Binary Anomaly Flag Data

Mulugeta Weldezigina Asres^{1*}, Christian Walter Omlin² and
The CMS-HCAL Collaboration^{3†}

^{1,2}Department of ICT, University of Agder, Grimstad, Norway.

³The CMS Experiment, CERN, Geneva, Switzerland.

*Corresponding author(s). E-mail(s): mulugetawa@uia.no;

Contributing authors: christian.omlin@uia.no; ;

†Full author list is provided at the end of the manuscript.

Abstract

Extracting anomaly causality facilitates diagnostics once monitoring systems detect system faults. Identifying anomaly causes in large systems involves investigating a broader set of monitoring variables across multiple subsystems. However, learning graphical causal models (GCMs) comes with a significant computational burden that restrains the applicability of most existing methods in real-time and large-scale deployments. In addition, modern monitoring applications for large systems often generate large amounts of binary alarm flags, and the distinct characteristics of binary anomaly data—the meaning of state transition and data sparsity—challenge existing causality learning mechanisms. This study proposes an anomaly causal discovery approach (ANOMALYCD), addressing the accuracy and computational challenges of generating GCMs from temporal binary flag datasets. The ANOMALYCD presents several strategies, such as anomaly data-aware causality testing, sparse data and prior link compression, and edge pruning adjustment approaches. We validate the performance of the approach on two datasets: monitoring sensor data from the readout-box system of the Compact Muon Solenoid experiment at CERN, and a public dataset from an information technology monitoring system. The results on temporal GCMs demonstrate a considerable reduction of computation overhead and a moderate enhancement of accuracy on the binary anomaly datasets. Source code: <https://github.com/muleina/AnomalyCD>

Keywords: Causal Discovery, Graphical Causal Modeling, Root Cause Analysis, Anomaly Detection, Time Series, Binary Data, Compact Muon Solenoid

Acronyms

<i>AD</i>	Anomaly Detection	<i>Bdeu</i>	Bayesian Dirichlet Equivalent Uniform Prior
<i>ANAC</i>	Our Anomaly Aware CI Test	<i>BN</i>	Bayesian Network
<i>AnomalyCD</i>	Our Anomaly CD Approach	<i>CD</i>	Causal Discovery
<i>APRC</i>	Area under Precision-Recall Curve	<i>CI</i>	Conditional Independence
<i>BIC</i>	Bayesian information criterion	<i>CMS</i>	Compact Muon Solenoid

<i>CP</i>	Conditional Probability	Θ	Moving Standard Deviation OD
<i>CPD</i>	CP Distributions	\mathcal{L}	Trend Deviation OD
<i>DAG</i>	Directed Acyclic Graph	Φ	Spectral OD
<i>DL</i>	Deep Learning	λ	OD Flag Generation Threshold
<i>FCI</i>	Fast Causal Inference	\mathcal{P}	Probability Function
<i>FCM</i>	Functional Causal Model	\mathbf{PA}_i	Set of Parent Nodes of x_i
<i>FFT</i>	Fast Fourier Transform	\mathcal{H}	GCM Extraction Function
<i>GAE</i>	Graph Autoencoder	$\hat{\mathcal{H}}$	\mathcal{H} using ANOMALYCD
<i>GCM</i>	Graphical Causal Model	\mathcal{I}	CI Test Function
<i>GES</i>	Greedy Equivalent Search	$\hat{\mathcal{I}}$	Anomaly-Aware CI Test Function
<i>GFCI</i>	Greedy Fast Causal Inference	ρ	Pearson's Correlation
<i>GS</i>	Grow-Shrink	\mathbf{G}_0	Initial \mathbf{G} , Prior Link Assumption
<i>HCAL</i>	Hadron Calorimeter	$\hat{\mathbf{G}}_0$	\mathbf{G}_0 after \mathcal{S}_e
<i>HE</i>	HCAL Endcap Detector	Γ_e	Edge Pruning Adjustment Function
<i>HEM</i>	HE Minus Hemisphere RBX	Λ	Binary Anomaly Flag Data
<i>HEP</i>	HE Plus Hemisphere RBX	\mathcal{S}_d	Sparse Data Compression Function
<i>IAMP</i>	Incremental Association	\mathcal{S}_e	Sparse Link Compression Function
<i>LHC</i>	Large Hadron Collider	\mathcal{B}	BN Model
<i>MMHC</i>	Max-Min Hill Climbing	\wp	BN Inference Engine
<i>MMPC</i>	Max-Min Parents and Children		
<i>OD</i>	Outlier Detection		
<i>PC</i>	Peter-Clark		
<i>PCMCI</i>	Peter-Clark Momentary CI		
<i>PDAG</i>	Partial Directed Acyclic Graph		
<i>QIE</i>	Charge Integrating and Encoding		
<i>RBX</i>	Readout Box		
<i>RCA</i>	Root-Cause Analysis		
<i>RM</i>	Readout Module		
<i>SDH</i>	Sparse Data Handling		
<i>SDLH</i>	Sparse Data and Link Handling		
<i>SHD</i>	Structural Hamming Distance		
<i>SHDU</i>	Undirected SHD		
<i>SiPM</i>	Silicon Photomultipliers		
<i>SR</i>	Spectral Residual		
<i>TPC</i>	Time-Aware PC		
<i>TS</i>	Time Series		
<i>VTTx</i>	Versatile Twin Transmitter		
x_i, X	Time series Data Variable(s)		
\mathcal{D}	Dataset, $X \in \mathcal{D}$		
$\hat{\mathcal{D}}$	Dataset after \mathcal{S}_d		
x_t	Trend component signal of x		
x_ζ	Seasonal component signal of x		
x_ε	Residual component signal of x		
p	Period of x		
τ_{max}	Maximum Time-Lag for CD		
l_m	Length Hyperparameter for \mathcal{S}_d		
\mathcal{G}	Graph with Nodes \mathcal{V} and Edges \mathcal{E}		
\mathcal{V}	Set of Nodes of \mathcal{G}		
\mathcal{E}	Set of Edges of \mathcal{G}		
ε	Graph Edge Link $\varepsilon \in \mathcal{E}$		
v, ν	Graph Node $v, \nu \in \mathcal{V}$		

1 Introduction

Anomaly detection (AD) approaches are commonly employed in industrial monitoring systems to capture anomalies that require attention [1–7]. Thus, improving efficiency, safety, and reliability, which will ultimately contribute to reducing maintenance cost and improving quality [1–10]. Discovering anomaly causality from a broader range of sensors, including variables not monitored by pre-trained AD models, is essential for facilitating fault diagnostics through root cause discovery and analysis. Causal knowledge of direct and indirect effects, interaction pathways, and time-lags can assist in comprehending the fault nature and modeling physical systems to predict the impact of anomaly occurrence or interventions [11].

The propagating nature of malfunctions makes fault diagnosis challenging in most multivariate processes [8, 12]. Causal knowledge of faults is traditionally acquired through inductive and deductive risk methods that employ variants of failure mode and effect analysis, and fault tree analysis, respectively [13]. These approaches provide rules for modeling expert knowledge for prior known malfunctions [14]. To effectively utilize these methods, an extensive domain knowledge from many experts is required, which is a

time-consuming process in addition to the possible ambiguity and incompleteness in large systems [13]. Data-driven approaches learn causality directly from the data collected by sensor monitoring systems [8, 15–21]. However, AD and causal discovery (CD) often remain highly intractable due to widely diverse operational modes, disparate data types, and complex fault propagation mechanisms [9, 16, 17]. Recent AD advances for large complex systems focus on specific subsystems due to the curse of dimensionality, data annotation challenges, and the need for accuracy improvement. This results in multiple AD models for monitoring different subsystems [1–7, 10]. Identifying the causes of an anomaly requires investigating an extensive set of monitoring variables across subsystems that the trained AD models do not cover. An end-to-end framework for anomaly CD that addresses the challenges pertaining to large systems, such as status data from multiple AD systems, dynamics set of monitored variables, and large temporal data, is thus of interest in various domains.

Graphical causal models (GCMs) provide an intuitive CD reasoning presentation for performing causal inference tasks, such as quantifying the causal strength of variables and root cause analysis (RCA) [22–25]. Refs. [26, 27] present a PCMCI method that is a state-of-the-art for GCM on TS data. The PCMCI combines a constraint-based Peter-Clark (PC) estimator with momentary CI algorithms to achieve good accuracy on large data sets [26–30]. Although the algorithm incorporates several multi-stage algorithms to reduce computation and improve convergence, the computation cost grows quickly for large datasets, limiting their adoption in real-time applications [31, 32].

We propose an anomaly causal discovery approach (ANOMALYCD) that integrates several methods to address computational and accuracy challenges related to generating causal knowledge discovery on multivariate TS anomaly data. We employ a temporal online AD method, sparse data handling, causal graph structure learning, and causality inference using probabilistic causal modeling. Our study focuses on discovering anomaly GCM from time series (TS) binary flags, as most monitoring systems log their data in this format. Binary flag data sets are widely available, and using them for CD lessens the impact of data

heterogeneity streamed from diverse AD models, providing data normalization. Although there are some recent efforts for inferring GCM from binary data [33] or outlier signals [24], there is still a gap in addressing the unique challenges of binary anomaly data for large systems. Temporal binary anomaly data has distinctive characteristics different from ordinary categorical or discrete data: 1) flag transitions between normal 0 and alert 1 have a meaning of anomaly occurrence and disappearance, and 2) data can exhibit severe sparsity because of long uniform status regimes leading to multicollinearity. The existing causality learning mechanisms have yet to be established effectively to handle these characteristics. Their accuracy suffers, and the computation cost grows quickly for large datasets, limiting their adoption in real-time applications. The ANOMALYCD leverages the accuracy and alleviates the computational burden of the PCMCI algorithm by customizing the conditional independence (CI) test, and sparse data and link compression algorithms to effectively capture temporal anomaly data attributes during graph structure generation. We propose simple but novel compression algorithms for binary flag data that substantially reduce the computational cost of the GCM learning process. Moreover, we enable a Bayesian network (BN) [34], as a probabilistic causal model, to query causality inference on the TS GCM.

We have applied the proposed approaches to multivariate sensor data from the readout box systems of the Hadron Calorimeter (HCAL) of the Compact Muon Solenoid (CMS) experiment at CERN’s Large Hadron Collider (LHC). The results establish that our approach accurately detects outlier behaviors and generates causal networks consistent with the actual physical circuit connections and environmental associations. We have also assessed and compared the efficacy of our approach with benchmarking state-of-the-art CD methods on a publicly available infrastructure monitoring dataset. The ANOMALYCD has improved the GCM accuracy and considerably improved the computational efficiency. Moreover, we have conducted an ablation study on ANOMALYCD to demonstrate the contribution of the proposed techniques. The key contributions of our study are highlighted below:

- We present an elaborate study on anomaly CD from binary TS data, discussing the impact of data characteristics on GCM and revealing potential limitations of existing approaches in the domain.
- We present ANOMALYCD for CD on anomaly flag data that addresses several graphical causal modeling challenges, such as anomaly-aware CI, data and initial non-coinciding edge compression, edge pruning, and adoption of BN for TS causality inference.
- We propose novel compression algorithms that significantly reduce the data size and graph edge search space of sparse binary data. The algorithms achieve promising computational efficiency that leverages speed and accuracy for graph structure learning, paving the way for online CD application.

We discuss the background on CD in Section 2. We briefly describe the HICAL readout box system and the public monitoring sensor data sets employed in the study in Section 3. We present our approaches in Section 4, and provide results and discussion in Section 5. We summarize the contribution of our study in Section 6. Finally, Appendix A presents algorithm pseudo-codes and Appendix B discusses further results.

2 Background

In this section, we will review anomaly CD approaches and graphical causal modeling, and highlight concepts of BN modeling.

In the realm of system monitoring for complex systems, it is imperative to delve beyond predictive or descriptive machine learning tasks to fully comprehend the cause-and-effect relationship among different variables and systems [16, 17]. The investigation of causality is a prominent area of interest in diverse fields, including but not limited to IT systems [22, 35], transportation [13], medical science [36, 37], meteorology [16], and social science [33]. Causal presentation of data is an essential component in RCA that deals with the identification of the underlying root causes and provides an explanation of how the faults are impacting the monitored system [24, 25, 35]. Causal models can answer diagnostic questions, such as what would happen if faults occur in

particular variables, and predict how specific variables trigger faults in other variables or systems.

The relationship among different variables or components often involves multiple time lags in modern cyber-physical industrial systems. These time lags delay the fault propagation on the causally connected process variables [38]. Although temporal data provides valuable context that enhances AD and CD, it can pose specific challenges, such as slower data acquisition rates than the underlying rate of changes in the causal processes, data non-stationarity, and causality heterogeneity and non-linearity (concept drift on the causal relationship) [15, 16].

2.1 Anomaly Causal Discovery

Recent data-driven approaches for CD and RCA include statistical [8, 19, 39–42], information theory [8], and machine learning algorithms [9, 17, 21, 38, 39]. Rashidi et al. [8] present kernel principal component analysis (KERNEL-PCA) transformation and symbolic transfer entropy to reduce causality analysis computation for RCA fault diagnosis on nonlinear variables. The proposed method identifies only potential root causes and does not provide causal interactions among TS variables. Tian et al. [19] propose convergent cross-mapping based on deterministic system theory to build a causal network for root cause tracing in industrial alarm data. Chen et al. [39] combine nonlinear chirp mode decomposition with Granger causality to analyze root causes for multiple plant-wide oscillations in a process control system. Liu et al. [17] employ a spatio-temporal pattern network for RCA on TS anomalies in distributed complex systems. The anomalies are detected from changes in the causality dependency networks generated from a model trained on a symbolic representation of the healthy TS data. Steenwinckel et al. [13] discuss fusing expert knowledge with a data-driven semantic rule mining (pattern matching using matrix profiling) for AD and RCA applied to predictive maintenance of trains. Liu et al. [41] discuss fine-tuning Spearman’s rank correlation analysis with domain knowledge rules to build a BN for fault detection and diagnosis. Qin et al. [40] utilize PCA for fault detection and variable importance selection using gradient boosting for RCA.

Recent approaches have also integrated causality inference into the AD deep learning models [21, 38]. Zhou et al. [21] present a temporal convolution and multi-head self-attention networks for CD and a contrastive causal graph for RCA. Chen et al. [38] propose a sparse causal residual neural network model to extract multi-time-lag causality for industrial process fault diagnosis. Leonhardt et al. [9] employ deep graph convolution neural networks to solve the sparse and nonlinear problem of the state space models for RCA.

GCMs are popular for their intuitive presentation of causality using graphs [22–25]. The graphs illustrate influence and effect paths, provide strength and direction of linkage, and enable estimation of influence propagation across their paths. These attributes make GCMs convenient for CD and RCA applications [24, 25]. Wang et al. [22] present CLOUDRANGER that utilizes the non-temporal PC algorithm for TS data to discover the causal graph between anomalies and identify root causes through a random walk on a correlation transition matrix. MICROCAUSE in Ref. [35] enhances the CLOUDRANGER by inferring the GCM using the PCMC algorithm [28]. WHYMDC in Ref. [23] identifies root causes from non-temporal data by searching for changes in causality on a given GCM. CAUSALRCA in Ref. [24] employs the SHAPLEY value [43] to quantify contributions and rank root causes of a point anomaly score using non-temporal structural causal models. EASYRCA in Ref. [25] identifies the root causes of collective anomalies using time of occurrence and divergence graph compared to the GCM built from normal operation. The study assumes that the graph already exists, which is a challenging assumption to hold in several real-world complex systems. The above recent approaches for anomaly RCA are not adequately optimized for binary anomaly-flag data CD, as they are limited to non-temporal modeling or require the availability of the GCM network [22–25]. Large complex systems often exhibit challenges, such as temporal fault propagation, the actual fault causal network is not readily available as the number of variables grows, and the fault network can differ from normal operation causal networks.

2.2 Review on Graphical Causal Discovery

The first step of graph-based causality analysis is to construct the GCM of the variables (see Definition 1).

Definition 1 *Graphical causal model (GCM)* states that if two variables have an edge in between $X \rightarrow Y$ in the directed graph, then X is a direct cause of Y ; there exist interventions on X that will directly change Y (distribution or value). The edge of GCM between variables X and Y can model 1) a direct causal relationship ($X \rightarrow Y$ or $Y \rightarrow X$), 2) a causal relationship in either direction ($X \leftrightarrow Y$), and 3) a non-causal ($X \leftrightarrow Y$) due to external common causes.

The GCM captures direct dependencies and shared drivers among multiple data variables, the graph nodes. Data-driven causal graph structure learning methods can broadly be categorized into:

- *Constraint-based*: Relies on conditional independence (CI) relationships $X \perp\!\!\!\perp Y|Z$ (X independent of Y condition on Z) to infer the causal directed acyclic graph (DAG) structure. Some of the popular methods include PC [36], grow-shrink (GS) [44], incremental association (IAMP) [45], max-min parents and children (MMPC) [46], and fast causal inference (FCI) [36]. The PC algorithm in Refs. [36, 47] is a widely used method that builds a causal graph by adding edges based on CI tests. It learns a partial DAG (PDAG) representing the dependencies based on the causal Markov condition and the faithfulness assumption. With no latent confounder, two variables are directly causally related with an edge in between if and only if there is no subset of the remaining variables conditioning on which they are independent.
- *Score-based*: Employs optimization search for causal DAG structure to the observed data based on a scoring metric [11, 15, 16, 48]; e.g., hill-climbing search (HC) [49], and greedy equivalent search (GES) [50, 51]. These methods explore the space of PDAG structures and minimize a global score—e.g., the *Bayesian information criterion (BIC)* and *Bayesian Dirichlet equivalent uniform prior (BDeu)*—using add, remove, and reverse

edge operators to return the optimal structure [50, 51].

- *Hybrid*: Combines constraint- and score-based algorithms to enhance accuracy and computational efficiency; e.g., max-min hill climbing (MMHC) [48], and greedy FCI (GFCI) [52]. The approaches build a first sketch of the graph using CI tests, and then orient the edges through score metrics or vice versa.
- *Functional causal model (FCM)*: is a recent CD approach that represents the effect as a function of the causes and independent noise terms [48, 52]; e.g., causal additive models [53] and causal generative neural networks [54] and others [15, 16]. FCM captures the asymmetry between cause and effect variables, representing the effect Y as a function of the direct causes X and noise factor ϑ as:

$$Y = f_{\theta}(X, \vartheta; \theta), \quad (1)$$

where ϑ is the noise term that is assumed to be independent of X , the function f explains how Y is generated from X , and θ is the parameter set of f .

Structured reviews on graph learning methods for GCM are available in Refs. [15, 16], and a more detailed explanation of structural causal model properties in a textbook [55]. We limit our discussion to studies related to TS data as in Refs. [11, 20, 21, 26–29, 38, 56–58].

2.2.1 Causal Discovery in Time Series

Graphical causal modeling for TS data is a growing study area in several scientific disciplines [26, 56]. TS data have become abundant in several real-world domains with the proliferation of sensor networks, but finding the causal dynamics in such data is challenging due to the temporal dependency, data non-linearity and non-stationarity, concept drift over time and varying data rates [15]. Time series GCM approaches need to capture time-lag causality (see Figure 1).

References [11, 26–29] introduce and extend variants of PCMCI, an extension of the PC algorithm [36] leveraged with false-positive cleaning momentary conditional independence for TS

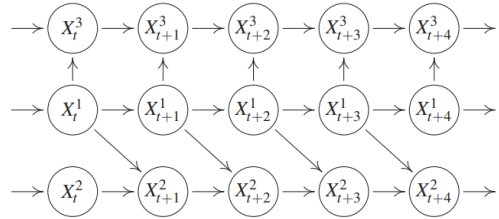


Fig. 1: A TS with time lag effect $\mathbf{x}_{t-1}^1 \rightarrow \mathbf{x}_t^2$ and instantaneous effect $\mathbf{x}_t^1 \rightarrow \mathbf{x}_t^3$ [55].

CD. The PCMCI methods with linear and non-linear conditional independence tests outperform state-of-the-art techniques in causality detection on large TS data sets across a range of research fields [28]. Gerhardus et al. [11] propose Latent-PCMCI that relaxes the causal sufficiency assumption of PC and extends PCMCI to enhance recall CD with unknown latent confounders using FCI. Saggioro et al. [29] extend the PCMCI to handle non-stationarity with regime-dependent GCMs using a time-windowing method. A slightly different approach is adopted in the time-aware PC (TPC) that employs the PC algorithm for TS by considering time delay, bootstrapping, and pruning [58]. The approach unrolls the TS data (adding new nodes with time delay tags) and generates a DAG by applying a set of conditions. Nauta et al. [20] present a temporal CD framework that consists of independent prediction convolutional networks for each variable, and attention scores are employed to infer the causal links among the variables. Training prediction models for each variable can constrain scalability when the number of variables increases, which is often the case in large complex systems.

2.3 Bayesian Networks

Probabilistic parameterization methods, such as BNs, allow flexible and faster querying for causal inference after building the causal topology structure. A BN is a probabilistic graphical model representing variables and their conditional dependencies through a DAG [34]. BNs are parameterized using *conditional probability distributions* (CPD), and each node x_i in the network is modeled as $\mathcal{P}(x_i|\mathbf{PA}(x_i))$, where \mathcal{P} is a probability operator, and $\mathbf{PA}(x_i)$ represents the parents of the node x_i in the network.

Definition 2 A *Bayesian network (BN)* is a probabilistic representation of joint distributions over the variables using a DAG model. The CPD is computed using the DAG from data using Bayes and the chain rules of probability as:

$$\mathcal{P}(A, B, C) = \mathcal{P}(A|B, C)\mathcal{P}(B|C)\mathcal{P}(C). \quad (2)$$

where the equation shows that the joint distribution of the variables is the sum of the CPDs in the network. Methods, such as the *Maximum likelihood estimation* and *Bayesian parameter estimator*, are widely employed BN learning techniques [49]. The maximum likelihood estimates the CPDs simply using the relative frequencies with which the variable states have occurred. The Bayesian parameter estimator mitigates the overfitting issue of relative frequencies (e.g., not fully representative data) using prior histogram counts, such as the *BDeu* to reflect a uniform distribution over possible values [49].

3 Dataset Description

This section briefly describes the data sets discussed in our CD study.

3.1 Dataset from the HCAL

The HCAL is a specialized calorimeter that captures hadronic particles during a collision event in the CMS experiment (see Figure 2) [59, 60]. The primary purpose of the HCAL is to measure the energy of hadrons by absorbing their energy and converting it into measurable signals. The calorimeter is composed of brass and plastic scintillators, and the scintillation light produced in the plastic is transmitted through wavelength-shifting fibers to *Silicon photomultipliers* (SiPMs) (see Figure 3) [60, 61]. The HCAL front-end electronics consist of components responsible for sensing and digitizing optical signals of the collision particles. The front-end electronics are divided into sectors of *readout boxes* (RBXes) that house and provide voltage, backplane communications, and cooling to the data acquisition electronics.

The HCAL is made of four subsystems (sub-detectors): the HCAL Endcap (HE), the HCAL Barrel (HB), the HCAL Forward (HF), and the HCAL Outer (HO) [63]. The front-end electronics of the HE, the main use-case of our study, is made

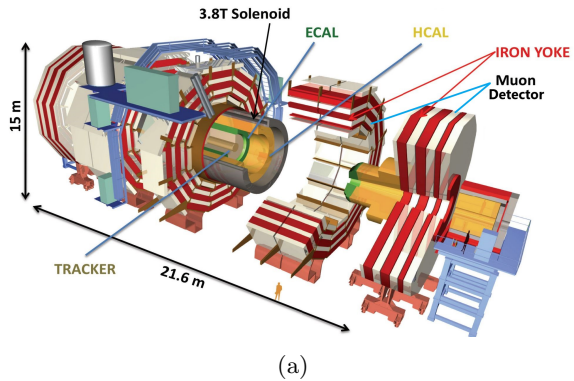


Fig. 2: Schematic of the CMS experiment [62]

of 36 RBXes arranged on the plus and minus hemispheres of the CMS detector [63, 64]. Each RBX houses four *readout modules* (RMs) for signal digitization [61]. Each RM has a SiPM control card, 48 SiPMs, and four readout cards—each includes 12 *charge integrating and encoding chips* (QIE11) and a *field programmable gate array* (Microsemi Igloo2 FPGA). The QIE integrates charge from each SiPM at 40 MHz, and the FPGA serializes and encodes the data from the QIE. The encoded data is optically transmitted to the backend system through the CERN *versatile twin transmitter* (VTTx) at 4.8 Gbps.

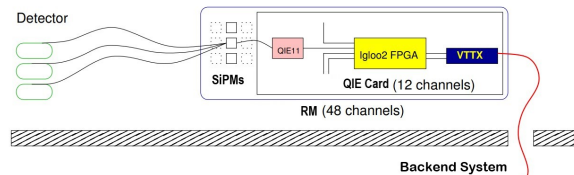


Fig. 3: The frontend electronics of the HE data acquisition chain, including the SiPMs, the front-end readout cards, and the optical link connected to the back-end electronics [61]. Each readout card contains twelve QIE11 for charge integration, an Igloo2 FPGA for data serialization and encoding, and a VTTx optical transmitter

The HCAL-RM dataset includes sensor readings from the RMs of the thirty-six RBXes in the HE detector. Each RM has twelve diagnostic sensors, four from the SiPM control card and eight from four QIE cards (see Table 1). The dataset was obtained from the HCAL online software monitoring system (the ngCCM server) from 01/08/2022 to 30/11/2022. The monitoring sensor

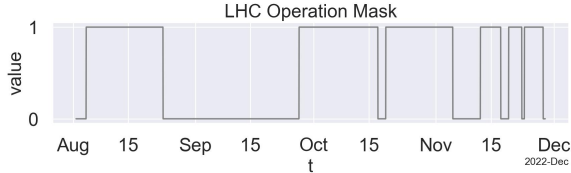


Fig. 4: The active mask of the LHC operation status from August to December of 2022. The active mask (1) refers to the LHC’s normal operation run during collision experiment or idle, whereas the inactive mask (0) for non-physics operation states, e.g., the LHC’s technical stop and maintenance

data comprises four-month data of 20.7M samples, around 12K per sensor per RM. The dataset contains irregularly sampled and considerably sparse data; a few samples are logged every eight hours for the SiPM control card and every two hours for the QIE card sensors. We utilize data from all four RMs (RM-1, RM-2, RM-3, and RM-4) of the RBX-HEP07, interpolated at one-minute interval for the online AD and CD evaluation. The RBX-HEP07 is one of the RBX with diverging behavior as discussed in the multivariate interconnection analysis study in Ref. [12].

Several extended reading gaps exist in the data due to various non-physics activities on the LHC. We generated a reading mask, shown in Fig. 4, to filter out the irrelevant regions of the LHC and ensure any detected anomalies are during the normal operation of the collider. The data comprise short-lived transient and time-persistent anomalies, such as trend drifts (see Figure 5). We employ data from multiple RMs to capture the global causality of the RM of the HE.

3.2 Dataset from EasyVista

EasyVista [65] has provided a multivariate sensor dataset from their information technology monitoring system and made the data publicly available in Ref. [66]. The dataset consists of eight TS variables collected with a one-minute sampling rate (see Table 2). Following Assaad et al. [25], we utilize a data segment, indexed from 45,683 to 50,000, for our CD evaluation, and each sensor is considered anomalous, exhibiting collective anomalies with close time of appearance and duration.

4 Methodology

This section presents our proposed ANOMALYCD approach for anomaly CD from TS data sets.

We present the ANOMALYCD for causality diagnostics that addresses the challenges of GCM of binary anomaly data sets. The system comprises two main modules, i.e., causal graph discovery and causality inference (see Fig. 6). The causal graph discovery generates temporal causal networks and trains a BN inference model on the anomaly data streamed from AD systems. The causality inference modules handle user queries with observation conditions to provide causality and conditional probabilities using the BN model.

We have previously trained deep-learning AD models on frontend electronics of the HE detector, including the *next-generation clock and control module* (ngCCM), RM, and *data quality monitoring* (DQM) [4–7]. The HCAL comprises several electronic components, and it is often essential to investigate multiple systems in the pipeline to diagnose system faults. We incorporate online temporal AD that detects anomalies on variables that are not actively monitored by trained models in Refs. [4–7]. Since previous works in Ref. [4–7] have already discussed the above-trained AD model, this study will focus on the proposed online AD and CD approaches.

4.1 Online Anomaly Detection

We present an online TS AD algorithm to detect outlier temporal patterns and generate anomaly flags for sensor variables that trained DL models do not actively monitor. Different types of variations can occur in TS data, including long-term trends, seasonal changes, periodic fluctuations, and non-random sources of variations [67]; these variations can impact the modeling approach and algorithm choices. Building a generic one-fits-all approach is challenging as the requirements depend on signal characteristics and target application. We propose online AD on univariate TS data to capture typical points and collective anomalies, including transient changes in time and frequency, and gradual signal trend drifts (see Algorithm 1 in Appendix A). The approach consists of an ensemble of time- and frequency-domain AD algorithms, presented at line 2 and line 3 in Algorithm 1, respectively. The final

Table 1: HE-RM monitoring sensor data variables description

No.	Notation	Variable Name	Description
1	SPV	PELTIER.VOLTAGE_F	Voltage of the SiPM Peltier temperature controller
2	SPC	PELTIER.CURRENT_F	Current of the SiPM Peltier temperature controller
3	SRT	RTDTEMPERATURE_F	SiPM control card temperature averaged over 50 samples
4	SCH	HUMIDITY_F	SiPM control card humidity
5	Q1H	1-B-SHT_RH_F	QIE card 1 humidity
6	Q2H	2-B-SHT_RH_F	QIE card 2 humidity
7	Q3H	3-B-SHT_RH_F	QIE card 3 humidity
8	Q4H	4-B-SHT_RH_F	QIE card 4 humidity
9	Q1T	1-B-SHT_TEMP_F	QIE card 1 temperature
10	Q2T	2-B-SHT_TEMP_F	QIE card 2 temperature
11	Q3T	3-B-SHT_TEMP_F	QIE card 3 temperature
12	Q4T	4-B-SHT_TEMP_F	QIE card 4 temperature

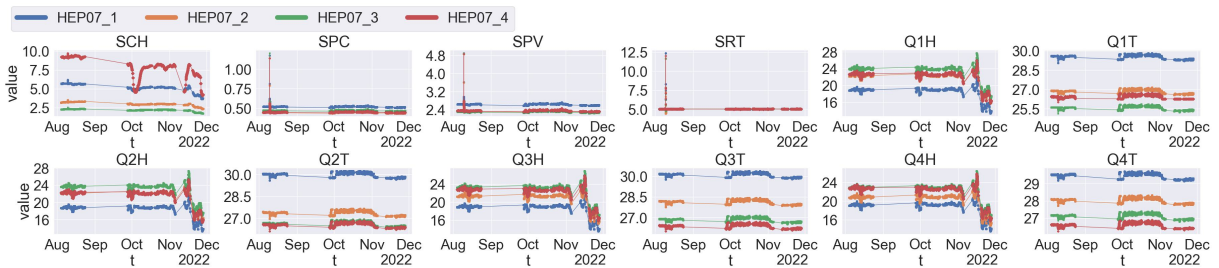


Fig. 5: Sensor TS data from all RMs of the RBX-HEP07. The HEP07_i denotes the i^{th} RM of the RBX

Table 2: EasyVista monitoring data variables description

No.	Notation	Description
1	PMDB	Extraction of message information received by the Storm ingestion system.
2	MDB	Activity of message orientation based on the type.
3	CMB	Activity of extraction of metrics from messages.
4	MB	Activity of insertion of data in a database.
5	LMB	Activity of updates of the last metrics values in Cassandra.
6	RTMB	Activity of searching to merge data with the check message bolt information.
7	GSIB	Activity of insertion of historical status in the database.
8	ESB	Activity of writing data in Elasticsearch.

binary AD flag data Λ is prepared using bit-wise union from each AD algorithm:

$$\Lambda = \Lambda_{\theta} \cup \Lambda_t \cup \Lambda_{\phi}, \quad (3)$$

where Λ_{θ} , Λ_t , and Λ_{ϕ} denote the temporal transient, temporal trend, and spectral AD flags, respectively.

4.1.1 Time-Domain AD

The Temporal AD detects transient temporal outliers and degradation in temporal trends on decomposed TS data (see in Algorithm 2). We apply *seasonal and trend decomposition* algorithm from Ref. [68] to estimate the trend and residual

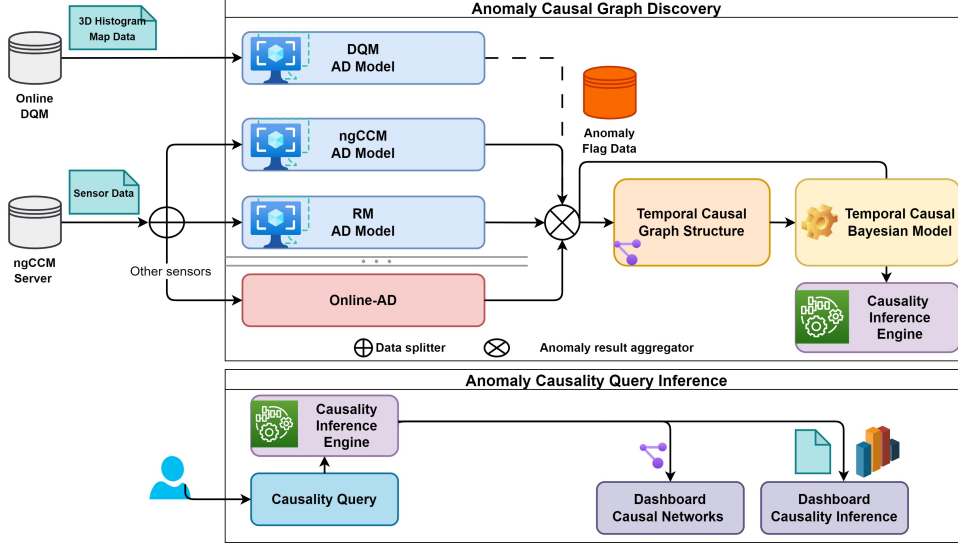


Fig. 6: ANOMALYCD: our anomaly CD approach with use-case of monitoring the HCAL systems. The online-AD detects anomalies on variables that are not actively monitored by the trained AD models of the HCAL, such as the *next-generation clock and control module* (ngCCM), *readout module* (RM), and *data quality monitoring* (DQM) AD models [4–7, 12]

signals, represented by x_l and x_ϵ , respectively:

$$\begin{aligned}
 x(t) &= x_l(t) + x_\zeta(t) + x_\epsilon(t), \\
 x_l(t) &= (h_p * x)(t), \\
 \text{where } h_p(t) &= \frac{1}{p}[1, 1, \dots, 1].
 \end{aligned} \tag{4}$$

The additive trend x_l is obtained by applying a convolution ($*$) filter h_p (a moving average with period p) to the data. The average of the de-trended series $x(t) - x_l(t)$ (after trend removal) over each period returns the seasonal component x_ζ . The final remaining component of the TS becomes the residual error x_ϵ . We employ *fast Fourier transform* (FFT) on $\Delta x(t) : x(t) - x(t-1)$ to enhance the accuracy of the period p estimation in the presence of additive trends (see line 3 in Algorithm 2 in Appendix A). The decomposition method in Eq. (4) assumes an additive trend and single seasonality or cyclic pattern. Other techniques, such as multiplicative trend or multi-seasonal component decomposition, can also be utilized depending on the expected normal signal characteristics [69].

We utilize a sliding z-score algorithm to generate Λ_θ from x_ϵ for the transient temporal AD (see Θ at line 5 in Algorithm 2). The x_ϵ signal

is normalized by subtracting the average μ_w and dividing it by the standard deviation σ_w using a sliding time-window (w_θ) to generate the AD score λ_θ (see line 11). The sliding window localizes the AD to the signal characteristics at adjacent TS data points. The μ_w and σ_w can be sensitive to strong outliers in the data, reducing AD efficacy, and it exacerbates for smaller sliding windows. Thus, we utilize data quantiles $Q = [10\%, 90\%]$ along with median centering, instead of mean, to reduce the influence of outliers on the μ_w and σ_w estimation (see line 10). Finally, we apply a threshold on the AD score to generate the AD flags Λ_θ (see line 12).

We develop a cumulative-based algorithm to detect drifts and generate Λ_l from the trend signal x_l (see \mathcal{L} at line 6 in Algorithm 2). We estimate first the trend score λ_l using a cumulative sum on the first-order difference of the x_l (see lines 13–21). The \mathcal{L} is designed to detect gradual signal drifts, and the trend score thus gets reset when during significant signal jumps or drops, often occurs during system configuration or maintenance updates. The z-score and spectral methods capture such sudden shifts. We apply the threshold α_l to get the trend drift AD flags Λ_l (see line 21).

4.1.2 Frequency-Domain AD

We employ spectral residual (SR) saliency detection to identify frequency spectrum or data rate change outliers (see Algorithm 3 in Appendix A). The SR method has been employed as a preprocessing technique for cleaning outliers and transforming data in semi-supervised AD research, as demonstrated in Refs. [4] and [70], respectively. The SR algorithm consists of three major steps for a given univariate data $x(t)$ [70]: 1) FFT \mathfrak{F} to get the log amplitude spectrum; 2) calculation of spectral residual; and 3) inverse FFT \mathfrak{F}^{-1} that transforms the data back to the time domain and generate saliency AD scores:

$$\begin{aligned} A(f), P(f) &= \mathfrak{F}(x(t)), \\ \bar{A}(f) &= \log(A(f)), \bar{A}_h(f) = h_q(f) * \bar{A}(f), \\ R(f) &= \bar{A}(f) - \bar{A}_h(f), \\ \Phi(x(t)) &= \|\mathfrak{S}^{-1}(\exp(R(f) + iP(f)))\|, \end{aligned} \quad (5)$$

where $A(f)$ is the amplitude spectrum; $P(f)$ is the corresponding phase spectrum; $\bar{A}(f)$ is the log representation of $A(f)$; and $\bar{A}_h(f)$ is the average spectrum of $\bar{A}(f)$ which can be approximated by convoluting with $h_q(f)$, where $h_q(f) = \frac{1}{q}[1, 1, \dots, 1]$ is averaging filter with an $1 \times q$ vector. $R(f)$ is the spectral residual, the difference between the log spectrum $\bar{A}(f)$ and the averaged log spectrum $\bar{A}_h(f)$. The data is transferred back to the time domain via \mathfrak{F}^{-1} to get the saliency signal ϕ . We apply a threshold α_ϕ to detect anomaly on λ_ϕ , normalized value of ϕ (see line 3) and generate the flags Λ_ϕ (see line 4).

4.2 Anomaly Causal Discovery

Graphical anomaly CD generates a DAG representing the causal interaction among the monitored variables. Computing a DAG for the temporal anomaly data in large systems pose computational and accuracy challenges due to large data size, high multidimensional and binary data sparsity leading to multicollinearity. We incorporate several methods to address these challenges using 1) data compression using multivariate sparse handling algorithm, 2) sparsity-driven prior link assumption compression, 3) anomaly flag-aware CI test, and 4) post-processing link adjustment.

The approach infers the temporal causal graph structure among monitoring variables or sensors

using time-lagged and contemporaneous CD algorithms. We employ PCMCI algorithm for its accuracy in temporal GCM on large data sets [27, 30] and propose augmentation algorithms to enhance its effectiveness for the particular challenges of large binary anomaly data. The PCMCI can result in spurious links due to errors in estimation when dealing with a long sequence of uniform binary anomaly regions among sensors due to multicollinearity [25, 71, 72]. The multicollinearity makes it difficult to assess the relative importance of highly correlated variables because of overlapping information, compromising the ability to infer a true GCM. Through sparse data and initial link assumption compression, CI testing sensitive to binary flag transitions ($0 \rightarrow 1$), and spurious edge pruning, we alleviate the computational cost and enhance the accuracy of causal graph building.

We leverage the PCMCI [11, 27] to learn the graph skeleton $\mathcal{G}(\mathbf{V}, \mathbf{E})$ from the Λ data, where \mathbf{V} is the set of sensor node vertices $v, \nu \in \mathbf{V}$, and $\mathbf{E} \subseteq \mathbf{V} \times \mathbf{V}$ is the set of edges $\varepsilon(v, \nu) \in \mathbf{E}$. The PCMCI, a constraint-based GCM methods, rely on CI tests to estimate links among variables. The independence score function $\mathcal{I}(X, Y)$ answers CI queries of the form $X \perp\!\!\!\perp Y|Z$ on a given dataset \mathcal{D} , where the variables are assumed to be generated independently from some (unknown) Bayesian system as:

$$\mathcal{I}(X, Y) : \mathcal{P}(X, Y|Z) = \mathcal{P}(X|Z)\mathcal{P}(Y|Z), \quad (6)$$

where the trade-off of controlling the Type I errors (false positives that reject true independence) and Type II errors (false negatives that accept false independence) is obtained by a significance level threshold $p_v > \alpha_p$ given an independence measuring function $f_{\mathcal{I}}(\mathcal{D})$, where $p_v = f_{\mathcal{I}}(\mathcal{D})$, probability of observing independence.

Let the PCMCI GCM extracting function is $\mathcal{H}(\mathcal{F}_t, \mathcal{I}, \mathcal{D}, \mathcal{G}_0)$, where \mathcal{F}_t is the temporal CD algorithm, \mathcal{I} is the CI test function, $\mathcal{D} \in \mathcal{B}^{n \times N}$ is the TS dataset with N variables and n data samples. The \mathcal{G}_0 is the initial search graph (prior link assumption) with all possible edges. The ANOMALYCD GCM extractor $\hat{\mathcal{H}}$ is formulated as:

$$\hat{\mathcal{H}}(\mathcal{F}_t, \mathcal{I}, \mathcal{D}, \mathcal{G}_0) = \Gamma_e \left(\mathcal{H}(\mathcal{F}_t, \hat{\mathcal{I}}, \hat{\mathcal{D}}, \hat{\mathcal{G}}_0) \right), \quad (7)$$

where $\hat{\mathcal{I}}$ is anomaly-aware CI testing function, $\hat{\mathcal{D}} = \mathcal{S}_d(\mathcal{D}, l_m)$ is compressed data after sparse data handling using \mathcal{S}_d and compression length hyperparameter l_m , and $\hat{\mathcal{G}}_0 = \mathcal{S}_e(\mathcal{G}_0, \hat{\mathcal{D}})$ is compressed prior link assumption after sparse link handling using \mathcal{S}_e . The Γ_e is the edge pruning function that removes spurious links from multiple time lags at the post-processing stage. We leave readers to Refs. [11, 27, 28] for a comprehensive explanation of the working principle of the PCMCI algorithm, as we constrain the remaining discussion to our study.

4.2.1 Causal Graph Generation

We aim to capture the causality linkages on binary anomaly data, particularly the transition from being healthy with flag 0 to experiencing an anomaly with flag 1. The popular CI tests for categorical data, such as statistical *G-squared* [73] and information-theory *conditional mutual information* tests [11], can not easily distinguish the significance of the anomaly transition behavior. These methods could result in incorrect causality inferred from the association influenced by the zeros instead of the ones.

We propose $\hat{\mathcal{I}}$, an anomaly-flag aware CI test (ANAC), using a partial-correlation that only considers links with positive associations corresponding to anomaly occurrence. The PCMCI estimates GCM of a anomaly flag Λ_i with a time-lagged function of the multivariate as:

$$\Lambda_i = \mathcal{F}(w_j(t-s), \Lambda_j(t-s)), \quad (8)$$

for $s = 0, \dots, \tau_{\max}$ and $j \in \mathbf{PA}_i$,

where the w is the time-lagged causal weights; the τ_{\max} is the maximum time-lag for causal inference; the \mathbf{PA}_i is the set of the parent nodes or variables of i ; the \mathcal{F} is a binary GCM function. The CI test influences w_j that positive w_j indicates a positive correlation with Λ_i , increasing together during anomaly occurrence, and its value indicates strength of the correlation. Thus, we enhance the PCMCI [27] with simple but effective ANAC to detect anomaly occurrence causality by excluding causal time-lags with $\hat{\mathcal{I}} : w_j \leq 0$.

The partial correlation is estimated through *linear ordinary least squares regression* and positive *Pearson's correlation* (ρ) CI test on the residuals. To test $X \perp\!\!\!\perp Y|Z$, first Z is regressed

out from X and Y using the regression model:

$$\begin{aligned} X &= \beta_X Z + \epsilon_X, \\ Y &= \beta_Y Z + \epsilon_Y, \end{aligned} \quad (9)$$

where ϵ_X and ϵ_Y are residuals, and their independence is evaluated using Student's t-test on the $\rho(\epsilon_X, \epsilon_Y)$ to generate the p_v . Finally, the set of $j \notin \mathbf{PA}_i$ are excluded based on union of the significance CI test and non-positive correlation as:

$$\hat{\mathcal{I}} : p_v > \alpha_p \cup w_j \leq 0. \quad (10)$$

4.2.2 Computation Cost of Graph Generation

The computational cost of GCM for TS data can vary with the number of variables N , the data sample size n , the maximum time-lag τ_{\max} , and the choice of conditioning set size $d = |Z|$ [26]. The overall processing cost depends on the cost of the employed CI test $\mathcal{K}_{\mathcal{I}}$ and the number of CI tests m that the CD algorithm executes to generate the GCM. The complexity of the CI test, $X \perp\!\!\!\perp Y|Z$: X independent of Y conditioned on Z , is one major factor affecting the computational workload in a constraint-based algorithm [26]. The cost of the GCM $\mathcal{K}(n, N, \tau_{\max})$ can be formulated as:

$$\mathcal{O}(\mathcal{K}) = \mathcal{O}(m \cdot \mathcal{K}_{\mathcal{I}}(n, N, \tau_{\max}, d)), \quad (11)$$

where $\mathcal{K}_{\mathcal{I}}$ is the cost per a single CI test with conditioning set size up to d . The computational complexity of the PC algorithm has been studied in Ref. [31]. Although the exact estimation of the cost is difficult [32], we briefly formulate the cost as follows. The cost per \mathcal{I} , a regression test using partial correlation, is $\mathcal{O}(\mathcal{K}_{\mathcal{I}}) = \mathcal{O}(nd^2)$, as the main cost comes from the matrix manipulation with dimension $d \ll n$. To simplify the mathematical formulation for m , let $\bar{N} = N \cdot \tau_{\max}$, approximating the number of variables in the temporal GCM. Considering CI tests without conditional set, i.e., $d = 0$, each variable $x_i \in \mathcal{D}$ will conduct $\mathcal{I}(x_i, x_j)$, for $\forall j \neq i$ and $t = [-\tau_{\max}, 0]$, resulting $\approx \bar{N}^2$ tests. Assuming the worst-case scenario where the PC tries all conditional sets $d = [0, \dots, \bar{N} - 2]$ and each d results in $\binom{\bar{N}-2}{d}$

selections, the m becomes:

$$m = \bar{N}^2 \sum_{d=0}^{\bar{N}-2} \binom{\bar{N}-2}{d} = \bar{N}^2 2^{\bar{N}-2}. \quad (12)$$

For a bounded scenario with fixed d , the above Eq. (12) reduces to:

$$m = \bar{N}^2 \binom{\bar{N}-2}{d}. \quad (13)$$

Thus, the final cost is approximated as:

$$\begin{aligned} \mathcal{O}(\mathcal{K}) &= \mathcal{O} \left(\bar{N}^2 \binom{\bar{N}-2}{d} n d^2 \right) \\ &= \mathcal{O} \left(N^2 \tau_{\max}^2 \binom{N\tau_{\max}-2}{d} n d^2 \right). \end{aligned} \quad (14)$$

The value of d depends strongly on the structure of the true GCM and the data characteristics. However, the typical value of d is small, ranging from 1 to 5, as sparsity is prevalent in most real-world graphs with few immediate parent nodes, and the majority of candidate links are eliminated quickly in the early steps before the CD algorithm reaches high-order conditioning sets. However, even with the integrated sparsity-based pruning mechanism of PCMCI algorithms, binary data with long uniform signals presents a challenge, such as multicollinearity, where variables influence several others, which impacts the partial correlation CI test, causing the d to grow and limit graph accuracy with many spurious links. Thus, optimizing computational efficiency by reducing the cost of the CT test function, $n \rightarrow n'$, and/or the number of CT tests, $N \rightarrow N'$, for a given τ_{\max} is beneficial.

4.2.3 Sparse Data Handling

Data sparsity is inevitable in binary anomaly data, as anomalies occur rarely and may persist over time when they appear. For large n , the computation overhead is significant. We exploit the anomaly data sparsity to reduce the sample data size of Λ using $\mathcal{S}_d(\Lambda)$ (see Algorithm 4 in Appendix A). The data compression lessens the computation to $\mathcal{O} \left(N^2 \tau_{\max}^2 \binom{N\tau_{\max}-2}{d} n' d^2 \right)$, where $n' \ll n$.

The sparse data handling (SDH) $\mathcal{S}_d(\Lambda)$ compresses the long regions with uniform anomaly status (see lines 3–9 in Algorithm 4). Hence, anomaly CD can be better captured (by reducing multicollinearity due to the sparse regions) from the status transitions with considerably lower computation on the compressed flag data Λ_c . The algorithm preserves the first l_m indices of the regions to capture the time-lag causality that ensures inference within time-adjacent anomaly occurrences while substantially reducing the size of the remaining sparse regions (see lines 7–8).

We set the time length l_m slightly greater than the causality searching τ_{\max} to avoid false adjacency between anomalies at different time stamps after compression. The l_m also regulates the contribution between collective trend drift anomalies and transient anomalies. Longer l_m increases the influence of the collective anomalies on the causality estimation and vice versa. Our method aims to reduce the n to address the computational burden of the GCM learning process on large datasets.

4.2.4 Sparse Graph Link Handling

The CD may remain complex for high-dimensional data with large N despite the reduction of the computation by \mathcal{S}_d [27]. Hence, we incorporate a sparse link handling algorithm \mathcal{S}_e that selects the initial prior links to reduce the searching space (see Algorithm 5 in Appendix A). The method aims to ameliorate the computation by reducing the number of conditional tests between potential links. The prior link assumption excludes self-lag links and links from non-coinciding variables on the binary anomaly data.

The assumption of self-lag exclusion $\mathbf{PA}_i \in \Lambda_j(t-s)$, $\forall j \neq i$ reduces the computation of the link search from $N^2 \tau_{\max}^2 \rightarrow N(N-1) \tau_{\max}^2$ (see line 2 in Algorithm 5). The assumption of non-coinciding link exclusion $\Psi(\Lambda_i, \Lambda_j) < \alpha_\tau$ excludes links from variables with temporally non-coinciding flags and alleviates the computation further, $N(N-1) \tau_{\max}^2 \rightarrow \sum_{i=1}^N N'_i \tau_{\max}^2$, where $N'_i \leq N-1$ (see lines 3–19). The $\Psi(\Lambda_i, \Lambda_j)$ measures the coincidence score $\lambda_\tau^{i,j}$ between the variables Λ_i and Λ_j and the threshold α_τ determines whether their link should be considered during the GCM learning phase.

Algorithm 5 starts by extending the anomaly flag regions by τ_{\max} (see line 4), as the GCM

search up to time lag of τ_{\max} , to calculate the coincidence score that measures the time-lagged co-occurrence among a pair of sensors (see lines 7–12). We first calculate the step-wise difference of binary flags $\Lambda(t) - \Lambda(t - 1)$ to detect the state transition regions (see line 3). We employ a sliding rolling sum with a window size of τ_{\max} and threshold the values above zero to create active windows (size of $\leq \tau_{\max}$) around the positive flag transitions (see lines 4–5). The $\lambda_r^{i,j}$ is calculated based on the normalized score of the number of co-occurring flags between the active windows of a pair of sensors (see lines 7–12). A link between i and j is not considered during the GCM learning phase if the $\lambda_r^{i,j} < \alpha_\tau$, e.g., zero indicates no co-occurrence (see lines 13–19).

4.2.5 Edge Pruning and Adjustment

Multiple sensor variables can report anomaly flags simultaneously for continuous time ranges that might cause the PCMCI [11, 27] to generate PDAG, which includes spurious edges—multiple time-lags, bidirected, or cyclic links—when dealing with temporal anomaly data. We present a pruning algorithm Γ_e as post-processing to overcome this challenge (see Algorithm 6 in Appendix A). The algorithm groups linked nodes and retains the lag with the highest weight or the earliest time-lag from the GCM. The higher link weights indicate stronger causality, and older time-lags correspond to earlier causality that is temporally close to the transitioning edges. We employ a *chi-square test* to direct the bidirected edges at $t = 0$ when the correlation CI test falls short in detecting the directions because of lack of time delay causality and symmetric correlation score unable to direct the edge. The pruning excludes the spurious links to generate a curated DAG that is needed for building the inference BN for causality query in the later stages.

4.3 Bayesian Network Modeling

We employ a BN to enable causality inference based on specific user query conditions beyond having a static graph skeleton. We utilize a *Bayesian parameter estimator* [49] with a *Bdeu* to learn the CPD parameters of the GCM. The edges of the generated temporal GCM $\mathcal{G}((v, \nu), \varepsilon(w, s))$ have weight w and time-lag s attributes. To build

a temporal causal BN, we reformulate as:

$$\mathcal{G}(\mathbf{V}, \mathbf{E}) : (v, \nu) \rightarrow (v_s, \nu), \varepsilon(w, s) \rightarrow \varepsilon(w_s), \quad (15)$$

where source node v with an edge $\varepsilon(w, s)$ is represented by new nodes v_s and an edge $\varepsilon(w_s)$ for every active time-lag s .

We prepare the data for training data for the BN by unrolling the TS data of the $v(t)$ (see Algorithm 7 in Appendix A). The approach is similar to the unrolling method adopted in TPC [58] for temporal GCM. New variable names with v_s tag for $v_s = v(t - s)$ are added by shifting the data ahead by the amount of time-lag s (see line 5–9). Although there are also other tools for building TS BN, such as dynamic BNs, most are restricted to 2-time step temporal BN that requires only a unit time-lag links ($\tau_{\max} \leq 1$) or existence of self-lag connections [74, 75].

5 Results and Discussion

This section presents the results of the performance evaluation of our ANOMALYCD and benchmark state-of-the-art methods on the HCAL-RM and EasyVista TS datasets.

5.1 Performance Metrics

We will employ visual illustrations and several quantitative metrics to evaluate the proposed approaches.

We will compute *structural hamming distance* (SHD) and *area under the precision-recall curve* (APRC) to compare the discovered causal DAGs quantitatively with the ground truth GCMs. The SHD is a standard distance metric that compares acyclic graphs based on the counts of the edges that do not match [48, 76]. It counts two errors for a directed link with the reversed edge: for falsely directing the edge and for missing the correct edge.

$$SHD(\mathcal{G}, \mathcal{Q}) \leftarrow \|\mathcal{G}(\varepsilon(i, j)) \neq \mathcal{Q}(\varepsilon(i, j))\| \quad (16)$$

for $(i, j) \in \mathbf{V}$,

where \mathbf{V} is the set of vertex nodes of the \mathcal{G} and \mathcal{Q} graphs, and $\|\cdot\|$ is a count function for the number of mismatched nodes between the \mathcal{G} and \mathcal{Q} .

The APRC is a classification metric that evaluates performance using the area under the curve

of the *precision* (P) and *recall* (R) coordinates. The P and R are defined as:

$$P = \frac{TP}{TP + FP}, \text{ and } R = \frac{TP}{TP + FN}, \quad (17)$$

where the TP, FP, and FN stand for true positive, false positive, and false negative, respectively: the TP is the number of edges estimated with a correct direction; the FP is the number of edges that are in the estimated graph but not in the true graph; the FN is the number of edges that are not in the estimated graph but in the true graph.

We will also utilize additional metrics, such as F_1 -score, *false positive rate* (FPR), and *undirected SHD* (SHDU), to compare the performance with benchmark CD approaches:

$$F_1 = \frac{2 \times P \times R}{P + R}, \text{ } FPR = \frac{RV + FP}{TN + FP}, \text{ and } \quad (18)$$

$$SHDU = UE + UM + RV,$$

where the SHDU penalizes edges with wrong directions once instead of twice like SHD in Eq. (16) [77]. The TN stands for true negative and is calculated as the number of edges that are neither in the estimated graph nor the true graph. The RV, UE, and UM denote the number of reversed edges, undirected extra edges, and undirected missing edges, respectively.

5.2 Causal Discovery on the HCAL

This section will discuss the performance of the proposed ANOMALYCD using a use case HCAL-RBX system. We will first discuss the performance of the online AD approach and then proceed to the anomaly CD.

5.2.1 Online Anomaly Detection

Table 3 provides the hyperparameter settings of the online algorithms incorporated in our ensemble AD approach. We set the anomaly thresholds slightly higher to reduce noise contamination and preserve the causal faithfulness assumption [15, 36, 54].

The LHC has undergone operations that result in distinct signal patterns on the sensors (see Fig. 4). We have thus utilized change point breaks (on 2022-09-27, 2022-10-19, and 2022-11-12) in

Table 3: Hyperparameter settings for the online AD.

Algorithm	AD Settings
Θ	$\alpha_\theta = 10, w_\theta = 5760$
\mathcal{L}	$\alpha_\tau = 20, p_\tau = 5760, k_\tau = 5$
Φ	$\alpha_\phi = 35, q_\phi = 1440$

which the AD reinitializes to deal with irrelevant data during operation interruptions.

Figure 7 depicts the SCH sensors of the four RMs of HEP07 along with the detected transient and trend anomalies marked on the AD score signals of the AD algorithm. The sensors exhibit drifting trends that gradually deviate from the expected optimal values. Figure 8 illustrates all the sensors from RM-1 with marked anomalies. The humidity sensors have higher anomaly flag counts due to the detected trend drift anomaly.

We have demonstrated the capability of our proposed online AD approach in detecting different types of anomalies on TS data with light computation overhead. The potential limitation of the approach is that it expects adequate healthy data samples, as it is challenging to detect anomalies without prior knowledge when the outlier is dominant in data that violates the rare anomaly occurrence assumption. In such cases, using trained AD models is recommended. Finding the optimal hyperparameters is another open challenge. Despite data normalization and standardization partially alleviating this challenge, hyperparameters tuning may require domain knowledge to capture the right data characteristics. However, hyperparameter adjustment on statistical models is lightweight and could be faster than tuning and retraining of DL models.

5.2.2 Graphical Causal Discovery

We capture the GCM from the TS binary anomaly data generated by the online AD algorithm in the previous section (see Fig. 9). We employ data from multiple RMs to capture the global causality of the RM of the HE. We set the $\tau_{\max} = 5$ to search for temporal causality dependency at $[t - \tau_{\max}, \dots, t]$ (equivalent to five minutes) and CI threshold $\alpha_p = 0.05$ for the PCMCI.

The sparse data handler \mathcal{S}_d reduces the data by 99.8% from approximately 400,000 to 900 samples. This greatly alleviates the computational

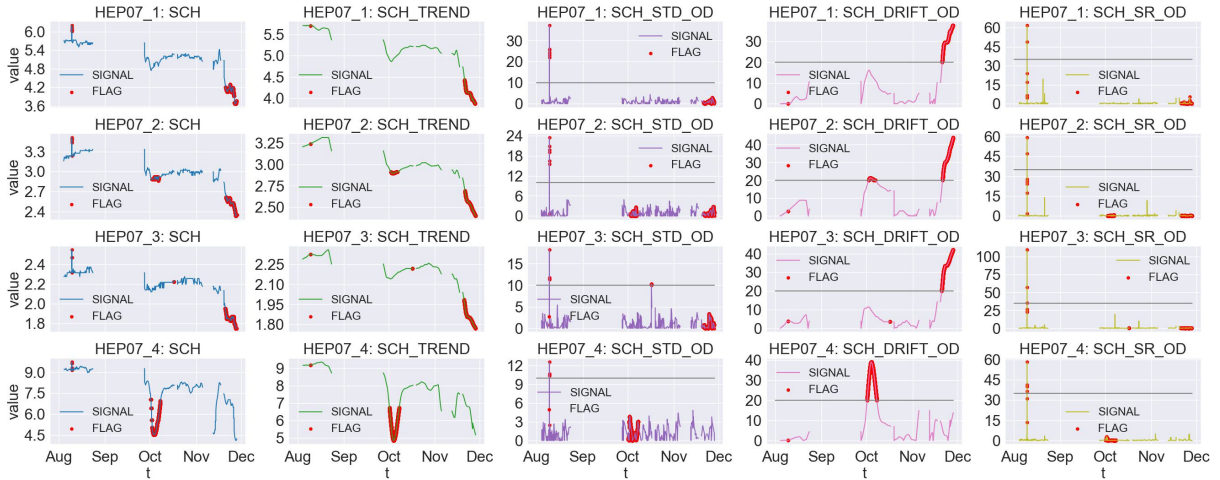


Fig. 7: Online AD on RBX-HEP07 SCH sensors. (Left to right) sensor signal, signal trend estimation, Λ_i of \mathcal{L} , Λ_θ of Θ , and Λ_ϕ of Φ

cost of the GCM learning [26, 27]. The \mathcal{S}_d took 8 seconds, and it squeezes the uniform regions to $l_m = 10$ samples, i.e., twice of the $\tau_{\max} = 5$ of the CD (see Fig. 9b).

We evaluate the discovered GCM by measuring the accuracy with respect to expected interconnection graph network depicted in Fig. 10. Figure 11a illustrates the temporal GCM structure on the time-lag of $t = [-\tau_{\max}, 0]$, captured by our ANOMALYCD method before edge link pruning. The GCM shows expected interconnection among the sensors: the clustering of environmental temperature and humidity sensors, and the link between the temperature regulator Peltier voltage and current, and the corresponding temperature sensors. Several bidirected edges with multiple time-lags are also present in the network. Figure 11b shows the final temporal DAG after applying Algorithm 6 for the pruning. An interesting time-lagged causality link can be observed, where a temperature anomaly in SRT leads to anomalies in SPV and SPC; this is because the Peltier regulator increases SPV and SPC to respond to SRT’s upsurge.

Table 4 presents quantitative performance of the graphical CD for the HCAL-RBX. The PDAG from the PCMCI algorithm, with spurious links at multiple time lags, leads to higher inaccuracy and lower performance. Our AnomalyCD has improved the CD substantially with a relative gain of 26.2% in F_1 , 74.9% in FPR, 17.1% in APRC, and 70.6% in SHDU. The ANAC delivers improvement of around 16% in F_1 , 44%–56% in FPR,

9%–12% in APRC, and 41%–53% in SHDU. The impact of edge pruning Γ_e remains limited when \mathcal{S}_e is employed, as most of the potential irrelevant edges are excluded by the \mathcal{S}_e . Further analysis of the CD over varying lengths of l_m is provided in the Appendix B.1.

Figure 12 portrays the computational cost of the CD using CPU processing time and incremental memory usage during the GCM learning phase. We conducted our experiment on 13th Gen Intel(R) Core(TM) i9-13980HX @ 2.2GHz with 64GB RAM. The PCMCI CD discovery on the raw data with over 400 thousand samples failed due to extremely slow processing. The ANOMALYCD with SDH \mathcal{S}_d consumes approximately 14 MB and executes in 9 seconds, with 99.8% compression in data size. The SDLH ($\mathcal{S}_d + \mathcal{S}_e$) contributes a further boost in memory and processing time by 14% and 27% as compared to the \mathcal{S}_d , respectively, by reducing the prior link assumption edges by 57.8%. We found the cost of Γ_e marginal with less than 0.5% increment in processing time.

5.2.3 Bayesian Causality Inference

We trained our BN model, the query engine for temporal GCM inference shown in Fig. 6, using unrolled TS data and the captured anomaly DAG skeleton. The causality queries on the BN include conditional probability (CP) inference, allowing users to query for the marginal distribution of anomaly occurrence. The inference enables estimating the causal effect between two

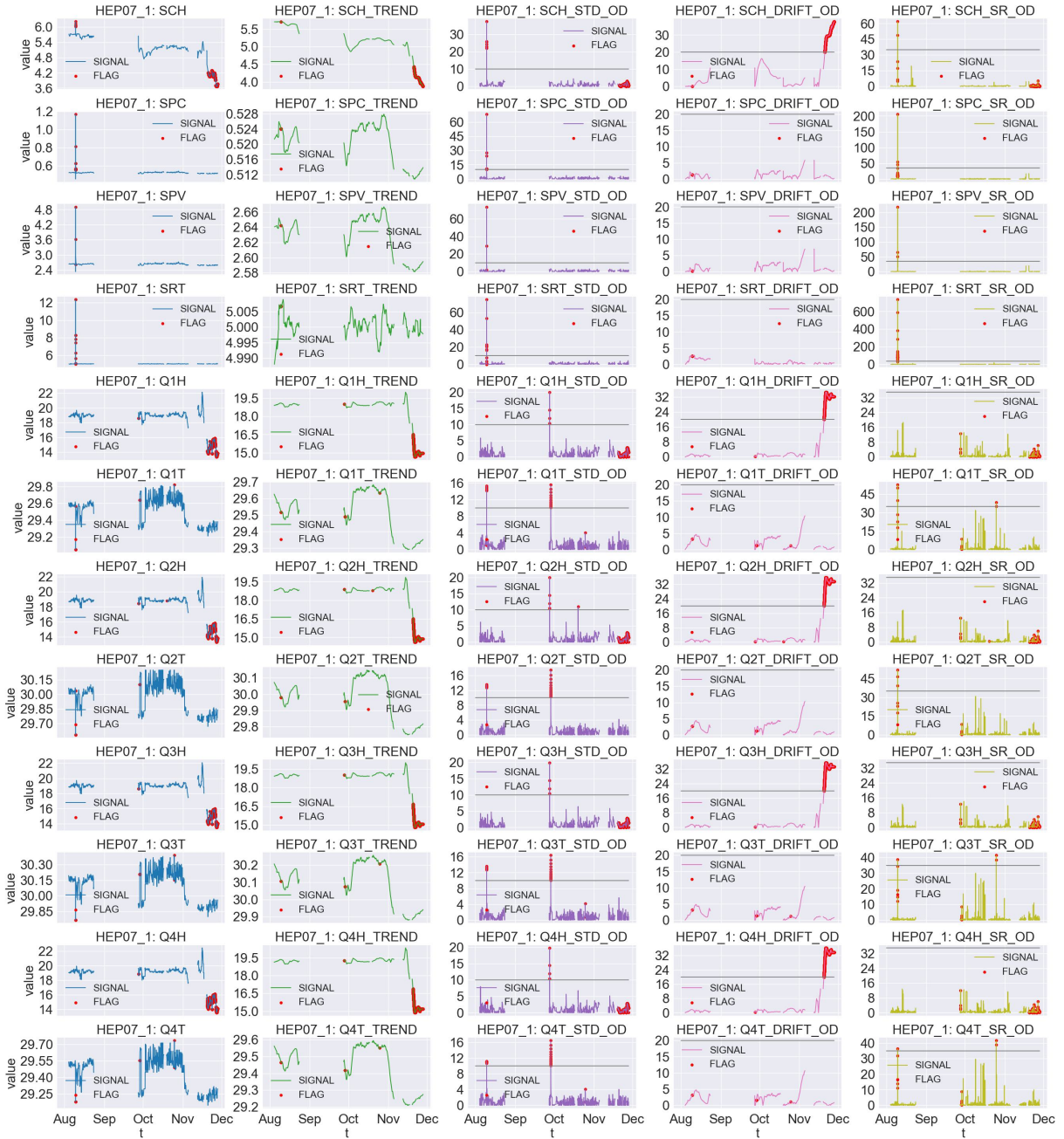


Fig. 8: Online temporal AD on the RBX-HEP07-RM-1 sensors

nodes given observed anomaly evidence on the others. We employ the *variable elimination* algorithm, an exact inference technique for solving Bayes' equations, to estimate CPs over a subset of variables from the probabilistic graphical BN models:

$$C_i = \varphi(\mathcal{M}_b, x_i, S), \quad (19)$$

where C_i is the CP of the $x_i \in \{0, 1\}$ sensor for its anomaly flag state $s_i = 1$ given the observed evidence on other sensors with states of $S = \{s_j \in \{0, 1\}, \forall j \neq i\}$. The φ is the inference engine with the BN model \mathcal{M}_b .

Table 5 presents results of anomaly causality inference queried from the \mathcal{M}_b . We quantify the causality by calculating the CP of the cause or

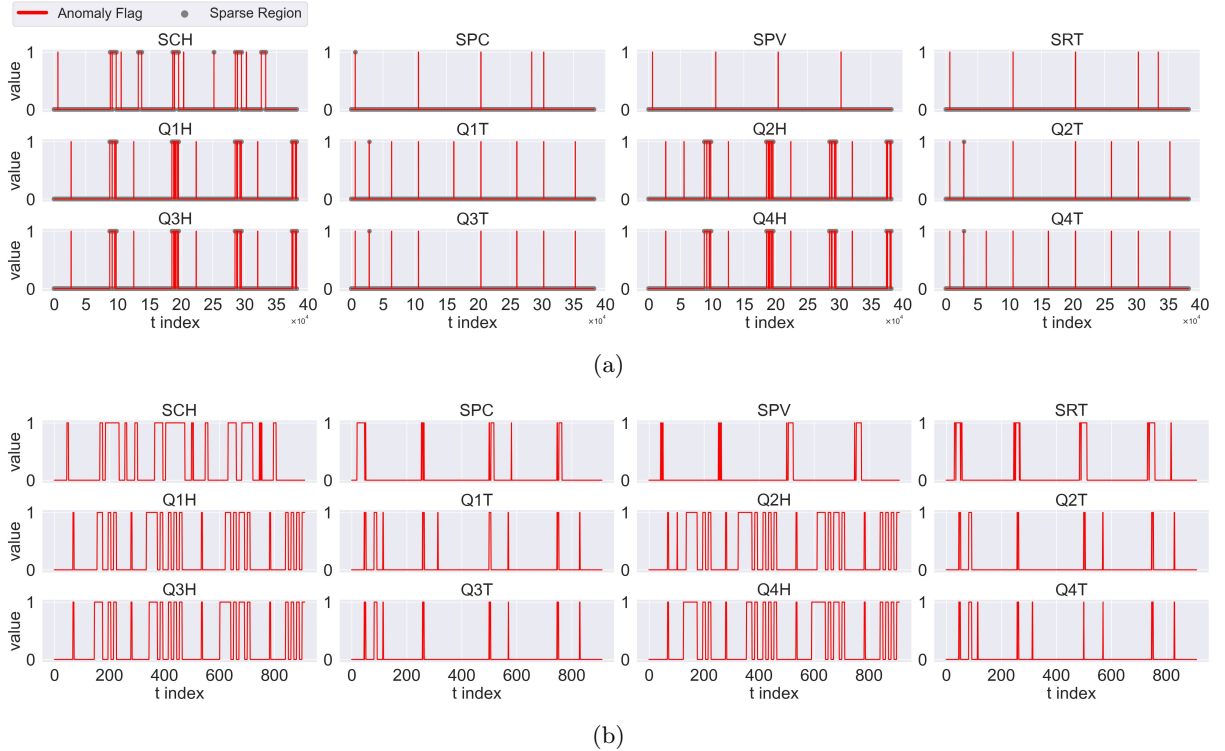


Fig. 9: Anomaly binary flag data from our proposed online AD approach on RBX-RM sensors: a) the raw anomaly data with approximately 4×10^5 samples and the sparse regions are annotated, and b) sparse compressed data through our \mathcal{S}_d with $l_m = 10$ and reducing the sample size to approximately 9×10^2

Table 4: Ablation study on ANOMALYCD graphical CD using HCAL-RM dataset. The ANOMALYCD: PCMCI + SDLH + ANAC + Edge Pruning. The SDH and SDLH denote \mathcal{S}_d and $\mathcal{S}_d + \mathcal{S}_e$, respectively. The PT is the processing time in seconds

Method	$F_1 \uparrow$	FPR \downarrow	APRC \uparrow	SHDU \downarrow	PT (secs) \downarrow
ANOMALYCD: PCMCI + SDH	0.667 (-)	0.410 (-)	0.730 (-)	17 (-)	9.148 (-)
ANOMALYCD: PCMCI + SDH + Edge Pruning	0.696 (4.3%)	0.410 (-)	0.741 (1.5%)	17 (-)	9.190 (0.5%)
ANOMALYCD: PCMCI + SDH + ANAC	0.774 (16.0%)	0.180 (-56.1%)	0.798 (9.3%)	8 (-52.9%)	8.966 (-2.0%)
ANOMALYCD: PCMCI + SDH + ANAC + Edge Pruning	0.800 (19.9%)	0.180 (-56.1%)	0.818 (12.1%)	8 (-52.9%)	8.997 (-1.7%)
ANOMALYCD: PCMCI + SDLH	0.725 (8.7%)	0.282 (-31.2%)	0.768 (5.2%)	12 (-29.4%)	6.641 (-27.4%)
ANOMALYCD: PCMCI + SDLH + Edge Pruning	0.719 (7.8%)	0.308 (-24.9%)	0.751 (2.9%)	13 (-23.5%)	6.680 (-27.0%)
ANOMALYCD: PCMCI + SDLH + ANAC	0.842 (26.2%)	0.103 (-74.9%)	0.855 (17.1%)	5 (-70.6%)	6.553 (-28.4%)
ANOMALYCD: PCMCI + SDLH + ANAC + Edge Pruning	0.842 (26.2%)	0.103 (-74.9%)	0.855 (17.1%)	5 (-70.6%)	6.588 (-28.0%)

The **black bold font** is the best score. The downarrow (\downarrow) means lower is better, and vice versa for uparrow (\uparrow). The percentages are calculated relative to the performance of the PCMCI + SDH.

affected sensors. The CP of anomaly occurrence for the Q1T sensor increases from 0.05 with no other evidence to above 0.90 with the evidence of a detected anomaly flag on the related Q[2-4]T sensors at a time-lag $t = 0$. The CP of an anomaly on the Q1H sensor increases from 0.26 to above 0.85 when there is evidence of a detected anomaly flag on the Q[2-4]H sensors at a time-lag of $t = 0$. The Q1H has a higher CP with no other evidence scenario due to trend drifts. We notice

that the few sample differences during drift detection across the Q[1-4]H sensors lower the causality dependency strength. The CP of SPC increases to 0.45 when SPV has an anomaly at $t = 0$. The SRT is causal to the SPC at a time-lag $t = -1$ directly and at $t = -5$ through SPV, but with uneven edge strength of 0.32 and 0.15, respectively. The CP rises to 0.95 on the SPC when anomalies are detected on both the SPV and SRT, indicating

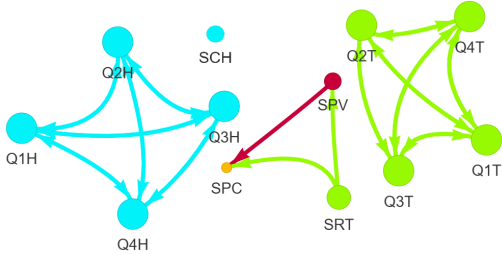


Fig. 10: Interconnection graph of the HCAL-RM system. We inferred the graph using domain knowledge of circuit connections, shared housing of the RM components, and the interconnection discovery result from Ref. [12]

the CP is influenced by edge weight strength from multiple causal nodes.

The BN inference has generally produced CPs that are aligned with the link strength of the causal DAG, depicted in Fig. 11b. But, caution should be taken when approaching the BN causality interpretation: 1) edges between Q[1-4]T and Q[1-4]H (sensors from the closely placed QIE cards) indicate the BN inference depicts the anomaly relationship rather than the causality between the sensors, and 2) CP, whether it is causal or influenced by observed evidence, must be explained with link edge direction; for example, the CP increase in the SPC is due to the anomaly on the causal SPV node, whereas the increase on the SPV is from its influenced on the SPC node.

5.3 Causal Discovery on EasyVista

We have tested our ANOMALYCD approach on a publicly available EasyVista dataset [66] (see Section 3.2). The dataset have been utilized the dataset for RCA study using a prior known causal graph network of the sensors [25](see Fig. 13).

Figure 14b presents generated the anomaly flags data using our online AD approach. We have utilized a low threshold $\alpha_\phi = 2$ to detect more outliers beyond the main collective anomaly at indices 46, 683–46, 783 to improve the CD learning. The EasyVista experts consider the PMDB and ESB variables, with the highest anomaly flags, as the root causes of the anomalies [25, 66].

We utilize the causal graph of the normal operation, given in Fig. 13, as a reference graph to evaluate the accuracy of the estimated GCMs. Table 6 presents some of the popular benchmarking CD methods in the literature. We have

preserved the undirected edges as bidirected for a fair comparison among the methods, as some of the methods generate PDAG. Since the ground truth graph does not contain temporal information, we convert the temporal GCM results into a summary GCM for the PCMCI temporal CD, i.e., we aggregate the time lag attributes of the edges into $t = 0$. We utilize partial correlation for the CI testing, and a threshold $\alpha_p = 0.05$ for the constraint-based methods. We employ BIC and BDeu scores [78] for the score-based algorithms.

Table 7 provide the CD performance on the raw and compressed anomaly data before and after \mathcal{S}_d , respectively. The \mathcal{S}_d reduces the data size to 1,900 samples (55% ↓), which lowers computation time by 8–10 times. It increases the accuracy of the causal graph by improving the precision (reducing false edges), which is demonstrated by the higher F_1 , and lower FPR and SHDU. The score-based HC [49] and its hybrid MMHC [48] algorithms have limited accuracy gain on the compressed data. Only the graph autoencoder (GAE) [83] has succeeded from the DL models. The RL-BIC [84] and CORL [85] employ reinforcement learning and have missed all relevant edges. Our \mathcal{S}_d achieves an average relative improvement of 18.31%, 22.05%, and 15.45% in the F_1 , FPR, and SHDU, respectively, compared to raw data.

We present an ablation study in Table 8 for the ANOMALYCD approach to demonstrate the efficacy of the additional complexity using \bar{I} , \mathcal{S}_d , \mathcal{S}_e and Γ_e methods in leveraging the PCMCI algorithm [27]. The ANOMALYCD has enhanced the CD with relative gain compared to the PCMCI F_1 score, FPR, and SHDU by 20.5%, 47%, and 41%, respectively, demonstrating improved GCM accuracy. The relatively lower APRC (−11.2%) is due to the relatively lower edge recall of ANOMALYCD, as the spurious links in the PCMCI inflates the APRC score on the raw data. However, the gain of removing false positives outweighs the missed false negatives, as the overall performance improved in the F_1 and SHDU. The correlation-based CI test can remain symmetric and fail to distinguish edge direction at $t = 0$ when there is no time-lagged factor. Thus, the ANOMALYCD is enhanced using chi-square CI test to directed the bidirected edges (see line 17 in Appendix Algorithm 6). This further improves the

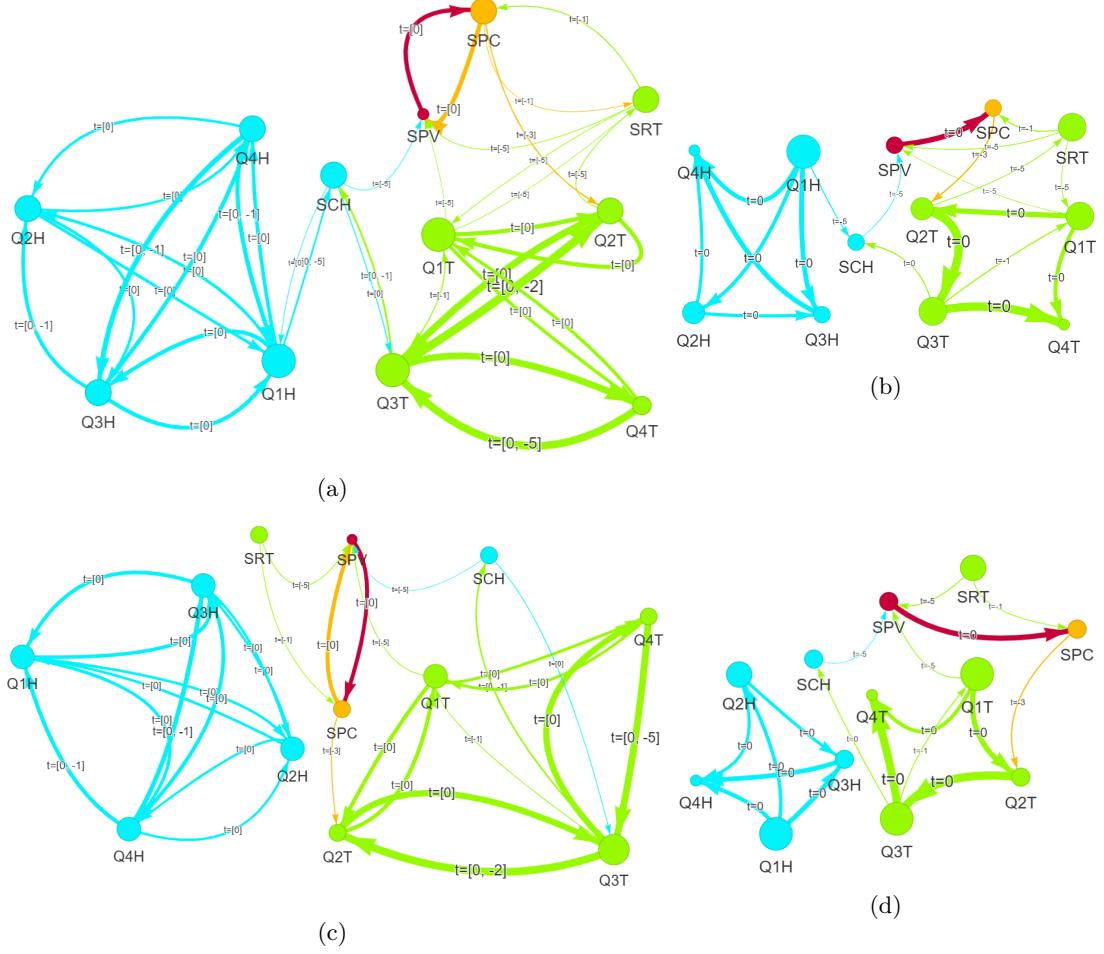


Fig. 11: Temporal GCMs of HEP07-RM using $\tau_{\max} = 5$ on time-lag $t = [-\tau_{\max}, 0]$: (top) with \mathcal{S}_d , and (bottom) with $\mathcal{S}_d + \mathcal{S}_e$. (a) and (c) are GCMs with PDAG before edge pruning, and (b) and (d) are GCMs with DAG after edge pruning

Table 5: Anomaly conditional probability \mathcal{P} based on Bayesian causality inference using pruned GCMs. The $A = 1$ and $B = 1$ denote the target and observed sensors with active anomaly flags

Target Sensor ($A = 1$)	Observed Sensors ($B = 1$)	$\mathcal{P}_{\text{SDH}}(A = 1 \mid B = 1)$	$\mathcal{P}_{\text{SDLH}}(A = 1 \mid B = 1)$
Q1T ($t = 0$)	-	0.051	0.052
Q1T ($t = 0$)	Q2T ($t = 0$)	0.904	0.906
Q1T ($t = 0$)	Q[2-4]T ($t = 0$)	0.927	0.928
Q1H ($t = 0$)	-	0.262	0.262
Q1H ($t = 0$)	Q2H ($t = 0$)	0.846	0.846
Q1H ($t = 0$)	Q[2-4]H ($t = 0$)	0.913	0.913
SPC ($t = 0$)	-	0.071	0.071
SPC ($t = 0$)	SPV ($t = 0$)	0.456	0.456
SPC ($t = 0$)	SRT ($t = -1$)	0.321	0.321
SPC ($t = 0$)	SPV ($t = 0$) and SRT ($t = -1$)	0.947	0.947
SPV ($t = 0$)	-	0.057	0.057
SPV ($t = 0$)	SPC ($t = 0$)	0.366	0.366

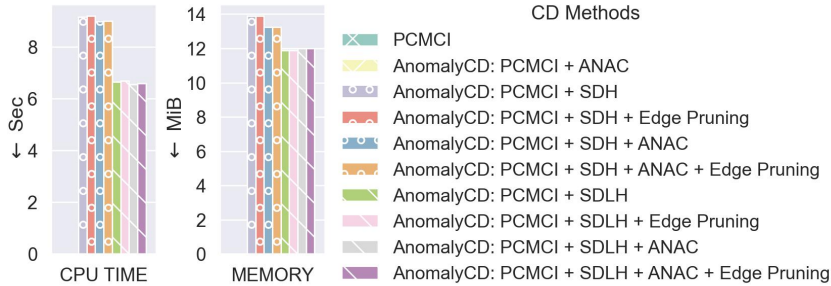


Fig. 12: Computational cost analysis on GCM learning on the HCAI-RM dataset. Our SDH \mathcal{S}_d reduces the data from 400 thousand (the PCMCI failed with extremely slow processing) to 900 (99.8% \downarrow) samples. The CD with \mathcal{S}_d consumes approximately 14 MB and executes in 9 seconds. The \mathcal{S}_e of the SDLH reduces the initial graph edges from 852 to 360 (57.8% \downarrow), resulting in a gain of 14% and 27% in memory and process time, respectively, as compared to the \mathcal{S}_d

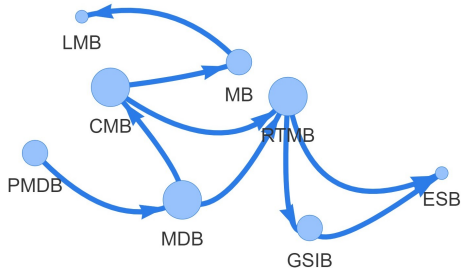


Fig. 13: Causal graph of EasyVista's monitoring system during normal operation

the cost of the pruning Γ_e negligible with less than 0.1% increment in processing time.

6 Conclusion

In this study, we have presented a novel scalable framework for discovering causal graphs from binary anomaly flag datasets. The framework incorporates various approaches to tackle the computational and accuracy challenges of inferring causality in sparse binary anomaly data. We have systematically integrated the characteristics of anomaly flag data into causal condition testing, sparse data compression, prior link compression, and pruning adjustments to achieve state-of-the-art computation efficiency and accuracy. The results of our experiments have demonstrated promising efficacy in unsupervised online anomaly detection and a significant reduction in the computational overhead associated with graphical causal discovery on time series data sets. Our approaches will facilitate real-time diagnostic tasks across various subsystems of large systems, such as the Hadron Calorimeter and other sectors related to Industry 4.0, addressing the demand for flexible, unsupervised, and lightweight approaches that are capable of handling complex and dynamic systems with limited annotated data sets. The tools presented in this study are deployed at CERN's Large Hadron Collider to provide anomaly detection diagnostics for the calorimeter systems.

Acknowledgements. We sincerely appreciate the CMS collaboration, the HCAL operation group, the HCAL publication committee, and

Table 6: Graphical causal discovery methods

Method Category	List of Methods
Constraint-based	PC [47], GS [44], IAMP [45], MMPC [46], PCMCI [27]
Score-based	HC [49], GES [50]
Hybrid-based	MMHC [48]
Function-based	Direct-LiNGAM [79], ICA-LiNGAM [80]
Gradient-based	GraN-DAG [81], GOLEM [82], GAE [83], RL-BIC [84], CORL [85]

F_1 is 0.381 (+26.2%), FPR is 0.421 (-53.0%), SHDU is 10 (-41.2%), and processing time is 7.567 (-89.9%). Figure 15 illustrates the GCM before and after directing the edges at $t = 0$ using chi-square test.

Figure 16 depicts the computational cost of the GCM learning, and our ANOMALYCD reduces the memory cost by half and the processing time by 10 times with 55% data compression. We found

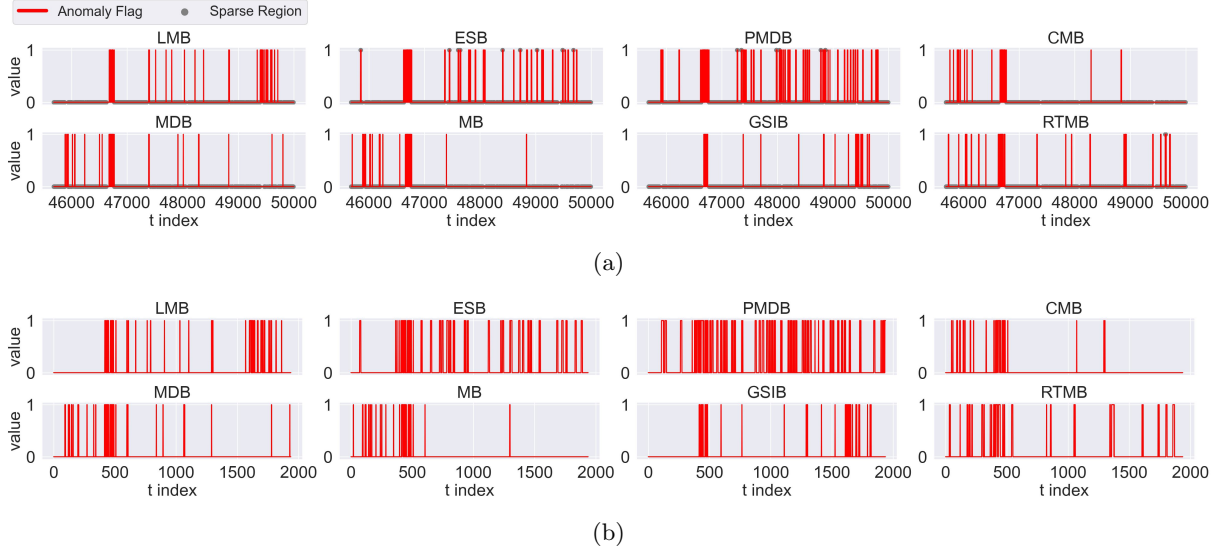


Fig. 14: The generated TS anomaly-flag data using our online AD on the EasyVista sensors: a) the raw anomaly data with approximately 4,300 samples and the sparse regions are annotated, and b) compressed data through our \mathcal{S}_d with $l_m = 10$ and reducing the sample size by approximately 55%

Table 7: Causal graph learning on the EasyVista dataset without and with (*) sparse handling

Method	Method Category	$F_1 \uparrow$	$F_1^* \uparrow$	FPR \downarrow	FPR* \downarrow	APRC \uparrow	APRC* \uparrow	SHDU \downarrow	SHDU* \downarrow
PC [47]	Constraint-based	0.154	0.333	0.790	0.474	0.395	0.225	18	12
GS [44]	Constraint-based	0.291	0.267	0.790	0.632	0.357	0.539	16	15
IAMB [45]	Constraint-based	0.291	0.267	0.790	0.632	0.357	0.539	16	15
MMPC [46]	Constraint-based	0.291	0.308	0.790	0.474	0.457	0.539	16	12
HC-BIC [49]	Score-based	0.191	0.100	0.526	0.526	0.164	0.249	13	15
HC-BDeu [49]	Score-based	0.296	0.148	0.737	0.842	0.221	0.372	17	19
GES-BIC [50]	Score-based	0.235	0.323	0.895	0.632	0.423	0.341	18	14
GES-BDeu [50]	Score-based	0.267	0.267	0.526	0.526	0.357	0.357	15	15
MMHC [48]	Hybrid-based	0.200	0.105	0.474	0.474	0.168	0.257	12	14
Direct-LiNGAM [79]	Function-based	0.242	0.222	1.050	0.790	0.297	0.345	21	17
ICA-LiNGAM [80]	Function-based	0.235	0.308	1.105	0.684	0.379	0.341	22	16
GOLEM [82]	Gradient-based	0.191	0.191	0.526	0.526	0.249	0.249	16	16
GraN-DAG [81]	Gradient-based	0.222	0.333	0.368	0.316	0.380	0.277	13	12
GAE [83]	Gradient-based	0.231	0.250	0.421	0.421	0.314	0.302	14	13
PCMCI [27]	Constraint-based	0.302	0.316	0.895	0.632	0.460	0.543	17	13
ANOMALYCD (ours)	Constraint-based	0.304	0.364	0.684	0.474	0.499	0.482	17	10

The **black bold font** is the best score. Downarrow (\downarrow) means lower is better, and vice versa for uparrow (\uparrow).

Table 8: Ablation study on our ANOMALYCD approach using the EasyVista dataset. The ANOMALYCD: the PCMCI is leveraged by sparse handling, ANAC, and edge pruning

Method	$F_1 \uparrow$	FPR \downarrow	APRC \uparrow	SHDU \downarrow	PT (secs) \downarrow
PCMCI [27]	0.302 (-)	0.895 (-)	0.543 (-)	17 (-)	74.667 (-)
ANOMALYCD: PCMCI + ANAC	0.304 (0.7%)	0.684 (-23.6%)	0.499 (-8.1%)	13 (-23.5%)	73.366 (-1.7%)
ANOMALYCD: PCMCI + SDH	0.316 (4.6%)	0.632 (-29.4%)	0.460 (-15.3%)	13 (-23.5%)	7.004 (-90.6%)
ANOMALYCD: PCMCI + SDH + Edge Pruning	0.333 (10.3%)	0.632 (-29.4%)	0.468 (-13.8%)	13 (-23.5%)	7.032 (-90.6%)
ANOMALYCD: PCMCI + SDH + ANAC	0.353 (16.9%)	0.474 (-47.0%)	0.477 (-12.2%)	10 (-41.2%)	6.571 (-91.2%)
ANOMALYCD: PCMCI + SDH + ANAC + Edge Pruning	0.364 (20.5%)	0.474 (-47.0%)	0.482 (-11.2%)	10 (-41.2%)	6.596 (-91.2%)
ANOMALYCD: PCMCI + SDLH	0.316 (4.6%)	0.632 (-29.4%)	0.460 (-15.3%)	13 (-23.5%)	6.207 (-91.7%)
ANOMALYCD: PCMCI + SDLH + Edge Pruning	0.333 (10.3%)	0.632 (-29.4%)	0.468 (-13.8%)	13 (-23.5%)	6.232 (-91.7%)
ANOMALYCD: PCMCI + SDLH + ANAC	0.353 (16.9%)	0.474 (-47.0%)	0.477 (-12.2%)	10 (-41.2%)	6.198 (-91.7%)
ANOMALYCD: PCMCI + SDLH + ANAC + Edge Pruning	0.364 (20.5%)	0.474 (-47.0%)	0.482 (-11.2%)	10 (-41.2%)	6.222 (-91.7%)

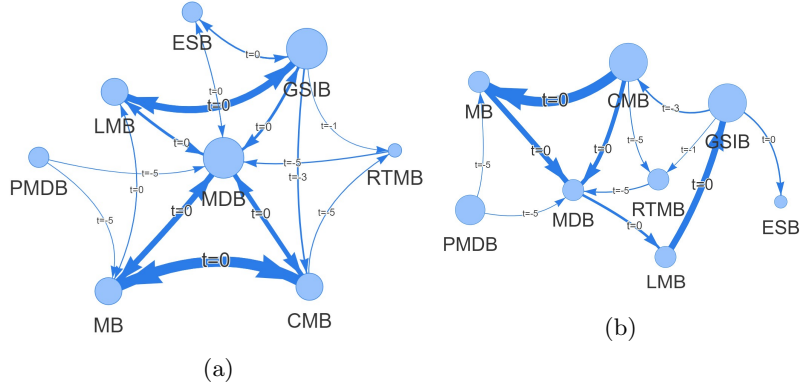


Fig. 15: The estimated TS GCM using ANOMALYCD on the EasyVista dataset: a) GCMs with PDAG before edge pruning at $t = 0$, and b) GCMs with DAG after edge pruning using chi-square test at $t = 0$

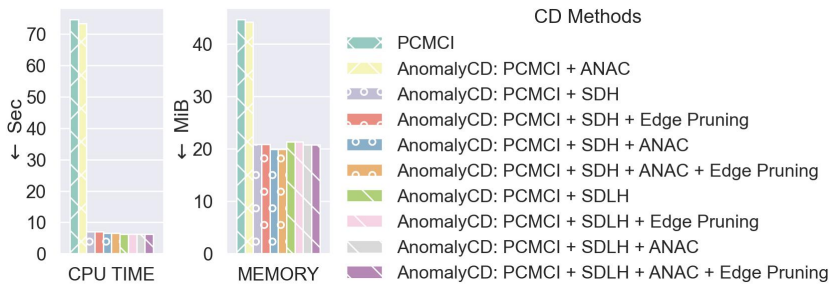


Fig. 16: Computational cost analysis on GCM learning on the EasyVista dataset. Our SDH \mathcal{S}_d compresses the data from roughly 4,300 to 1,900 samples (55% \downarrow), and the CD consumes 20 MB (53% \downarrow) and executes in 7 seconds (91% \downarrow). The \mathcal{S}_e of the SDLH reduces the initial edges from 376 to 324 (13.8% \downarrow) at $\alpha_\tau = 0.10$

the CMS machine learning teams. Their technical expertise, diligent follow-up on our work, and thorough manuscript review have been invaluable. We also thank the collaborators for building and maintaining the detector systems used in our study. We extend our appreciation to CERN for the operations of the LHC accelerator. The teams at CERN have also received support from the Belgian Fonds de la Recherche Scientifique, and Fonds voor Wetenschappelijk Onderzoek; the Brazilian Funding Agencies (CNPq, CAPES, FAPERJ, FAPERGS, and FAPESP); SRNSF (Georgia); the Bundesministerium für Bildung und Forschung, the Deutsche Forschungsgemeinschaft (DFG), under Germany’s Excellence Strategy – EXC 2121 ”Quantum Universe” – 390833306, and under project number 400140256 - GRK2497, and Helmholtz-Gemeinschaft Deutscher Forschungszentren, Germany; the National Research, Development and Innovation Office (NKFIH) (Hungary) under

project numbers K 128713, K 143460, and TKP2021-NKTA-64; the Department of Atomic Energy and the Department of Science and Technology, India; the Ministry of Science, ICT and Future Planning, and National Research Foundation (NRF), Republic of Korea; the Lithuanian Academy of Sciences; the Scientific and Technical Research Council of Turkey, and Turkish Energy, Nuclear and Mineral Research Agency; the National Academy of Sciences of Ukraine; the US Department of Energy.

Appendix A AnomalyCD Algorithms

The appendix presents our proposed algorithms for the online AD approach and the anomaly CD methods that are discussed in Section 4.

Algorithm 1 Online time series anomaly detection

```
1: procedure ONLINETEMPORALANOMALYDETECTION( $\mathbf{x}, p_\iota, \alpha_\theta, w_\theta, \alpha_\iota, k_\iota, \alpha_\phi, q_\phi$ )  
  ▷ Ensemble online TS AD  
  ▷  $\mathbf{x}$  is a univariate TS signal data  
2:    $\Lambda_\theta, \Lambda_\iota \leftarrow$  TEMPORALOUTLIERDETECTION( $\mathbf{x}, p_\iota, \alpha_\theta, w_\theta, \alpha_\iota, k_\iota$ ) ▷ for temporal outliers in the time domain  
3:    $\Lambda_\phi \leftarrow \Phi(\mathbf{x}, \alpha_\phi, q_\phi)$  ▷ for spectral outliers in the frequency domain  
4:    $\Lambda \leftarrow \Lambda_\theta \cup \Lambda_\iota \cup \Lambda_\phi$  ▷ union of binary outlier flags  
return  $\Lambda$ 
```

Algorithm 2 Time-domain AD

```
1: procedure TEMPORALOUTLIERDETECTION( $\mathbf{x}, p_\iota, \alpha_\theta, w_\theta, \alpha_\iota, k_\iota$ )  
  ▷ Temporal AD for temporal transient and gradual trend outliers in the time domain  
  ▷  $p_\iota$  is the window size of the convolutional filter for trend estimation  
2:   if  $p_\iota = \text{Auto}$  then ▷ for auto period estimation  
3:      $p_\iota \leftarrow$  SignalPeriodEstimation( $\mathbf{x}$ ) ▷ signal period estimation using FFT  
4:    $x_\iota, x_\zeta, x_\epsilon \leftarrow$  TimeSeriesDecomposition( $\mathbf{x}, p_\iota$ ) ▷ decomposition into a trend, cyclic and residual  
5:    $\Lambda_\theta \leftarrow \Theta(x_\epsilon, \alpha_\theta, w_\theta)$   
6:    $\Lambda_\iota \leftarrow \mathcal{L}(x_\iota, \alpha_\iota, k_\iota)$   
   return  $\Lambda_\theta, \Lambda_\iota$   
7: procedure  $\Theta(x_\epsilon, \alpha_\theta, w_\theta)$   
  ▷ Moving residual standard deviation for transient temporal AD  
  ▷  $\alpha_\theta$  is the detection threshold  
  ▷  $w_\theta$  is the sliding time-window size  
8:    $\lambda_\theta \leftarrow []$  ▷ placeholder for outlier flag data  
9:   for  $\mathbf{x}_w \in$  GetSlicedTimeWindowData( $x_\epsilon, w_\theta, \text{step} = 1$ ) : do ▷ data windowing  
10:     $\mu_w, \sigma_w \leftarrow$  GetStats( $\mathbf{x}_w$ ) ▷ median and standard deviation using quantile  $Q = [10\%, 90\%]$   
11:     $\lambda_\theta \leftarrow$  Append( $\lambda_\theta, |\mathbf{x} - \mu_w|/\sigma_w$ ) ▷ AD score  
12:    $\Lambda_\theta \leftarrow \lambda_\theta > \alpha_\theta$  ▷ temporal outlier flag  
   return  $\Lambda_\theta$   
13: procedure  $\mathcal{L}(x_\iota, \alpha_\iota, k_\iota)$   
  ▷ Cumulative sum-based trend drift AD  
  ▷  $\alpha_\iota$  is the detection threshold  
  ▷  $k_\iota$  is a scaling constant  
14:    $d_\iota \leftarrow \Delta(x_\iota) : x_\iota(t) - x_\iota(t-1)$  ▷ step change of trend data points  
15:    $\mu_{d_\iota} \leftarrow$  GetMedian( $|d_\iota|$ ) ▷ average step change on the trend  
16:    $\bar{d}_\iota \leftarrow |d_\iota| > k_\iota \mu_{d_\iota}$  ▷ check for large step changes in the trend  
17:    $\lambda_\iota \leftarrow$  InitializeWithZero( $\mathcal{L}(x_\iota)$ ) ▷ score placeholder with length of  $x_\iota, \mathcal{L}(x_\iota)$   
18:   for  $t_r, \bar{d}_{\iota r} \in$  GetUniformRegions( $\bar{d}_\iota$ ) : do ▷  $\bar{d}_{\iota r} \in \{0, 1\}$  is value of region  $r$ , and  $t_r$  is the time index of  $r$   
19:     if  $\bar{d}_{\iota r} = 0$  then  
20:        $\lambda_\iota[t_r[j]] \leftarrow \sum_{i=1}^j d_\iota[t_r[i]]$ , for  $j = [1, \dots, N_r]$  ▷ drift score using cumulative sum and  $N_r = \mathcal{L}(r)$   
21:    $\Lambda_\iota \leftarrow \lambda_\iota > \alpha_\iota$  ▷ trend outlier flag  
   return  $\Lambda_\iota$ 
```

Algorithm 3 Frequency-domain AD

```
1: procedure  $\Phi(\mathbf{x}, \alpha_\phi, q_\phi)$   
  ▷ Spectral residual (SR) for AD  
  ▷  $\alpha_\phi$  is the detection threshold  
  ▷  $q_\phi$  is siding spectral kernel size  
2:    $\phi \leftarrow$  SR( $\mathbf{x}, q_\phi$ ) ▷ outlier saliency score  
3:    $\lambda_\phi \leftarrow \frac{\phi - \bar{\phi}}{\bar{\phi}}$  ▷ normalized AD score  
4:    $\Lambda_\phi \leftarrow \lambda_\phi > \alpha_\phi$  ▷ spectral outlier flag  
return  $\Lambda_\phi$ 
```

Appendix B Further Results on Causal Graph Discovery

B.1 Causal Graph Discovery on the HCAL Dataset

The appendix presents a performance comparison of CD using different sparsity lengths l_m on the HCAL dataset. Figure B1 illustrates the data compression and CD performance trend with $\mathcal{S}_d + \mathcal{S}_e + \Gamma_e$ for $l_m = 5, 10, \dots, 50$. The results demonstrate a promising and consistent gain with

Algorithm 4 \mathcal{S}_d : Data compression on sparse binary anomaly flag

```
1: procedure  $\mathcal{S}_d(\Lambda, l_m)$ 
  ▷ Sparse (uniform no-state change) regions compression algorithm
  ▷  $\Lambda \in \mathbb{R}^{N \times T}$  is a matrix of anomaly flags with  $N$  sensors and  $T$  time length
  ▷  $l_m$  is the maximum time length for uniform states data compression
2:    $\Lambda_c \leftarrow []$  ▷ the placeholder for compressed data  $\Lambda_c \in \mathbb{R}^{N \times T_c}$ 
3:    $S \leftarrow \text{AggregateAnomalyState}(\Lambda)$  ▷ returns sequence of aggregated states of from all sensors
4:   for  $I, l_s \in \text{GetUniformRegions}(S)$  : do ▷  $I$  holds indices of the uniform region with a time length of  $l_s$ 
5:      $\Lambda_I \leftarrow \Lambda[I]$  ▷  $\Lambda_I$  is the selected uniform status flag region
6:     if  $l_s > l_m$  then
7:        $I_d \leftarrow \text{GetRangeToRemove}(\Lambda_I, l_m)$  ▷ the tail indices of the region, excluding the first  $l_m$  indices
8:        $\Lambda_I \leftarrow \text{CompressBinayData}(\Lambda_I, I_d)$  ▷ compressing time length of  $\Lambda_I$  by removing  $I_d$  data indices
9:      $\Lambda_c \leftarrow \text{Append}(\Lambda_c, \Lambda_I)$ 
return  $\Lambda_c$ 
```

Algorithm 5 \mathcal{S}_e : Sparse link handling with refined prior link assumption

```
1: procedure  $\mathcal{S}_e(\Lambda, \mathbf{E}, \tau_{\max}, \alpha_\tau)$ 
  ▷ Prior graph link preparation for GCM through removal of spurious and weak edges
  ▷  $\Lambda \in \mathcal{B}^{n \times N}$  is TS binary anomaly data
  ▷  $\mathbf{E} \subseteq N \times N$  is a prior assumption of time-lagged edge links, default is all
  ▷  $\tau_{\max}$  is the causality search maximum time-lag
  ▷  $\alpha_\tau$  is the time-lagged anomaly flag overlap strength threshold
2:    $\mathbf{E} \leftarrow \text{RemoveSelfTimeLagEdges}(\mathbf{E})$  ▷ remove all self time-lag edges from all the nodes
3:    $d\Lambda \leftarrow \Delta\Lambda : \Lambda(t) - \Lambda(t-1)$  ▷ transition of binary data
4:    $S_{d\Lambda} \leftarrow \text{ExtendAnomalyRegions}(d\Lambda, z = \tau_{\max})$  ▷ rolling sum with sliding window size  $z = \tau_{\max}$ 
5:    $\Lambda_\tau \leftarrow S_{d\Lambda} > 0$  ▷ convert to binary
6:   for  $\Lambda_\tau(i), \Lambda_\tau(j) \in \text{GetUniquePairSensors}(\Lambda_\tau)$  : do
7:      $\lambda_\tau \leftarrow \text{SimultaneousAnomalyCount}(\Lambda_\tau(i), \Lambda_\tau(j))$  ▷ number of overlapped flags between sensor  $i$  and  $j$ 
8:     if  $\lambda_\tau > 0$  then ▷ check if overlap exists
9:        $n^i \leftarrow \text{AnomalyCount}(\Lambda_\tau(i))$  ▷ total number of flags for sensor  $i$ 
10:       $n^j \leftarrow \text{AnomalyCount}(\Lambda_\tau(j))$  ▷ total number of flags for sensor  $j$ 
11:       $\lambda_\tau^{ij} \leftarrow \frac{\lambda_\tau}{n^i}$  ▷ normalized overlap score from  $i$  to  $j$ 
12:       $\lambda_\tau^{ji} \leftarrow \frac{\lambda_\tau}{n^j}$  ▷ normalized overlap score from  $j$  to  $i$ 
13:      if  $\lambda_\tau^{ij} < \alpha_\tau$  then
14:         $\mathbf{E} \leftarrow \text{RemoveEdges}(\mathbf{E}, i, j)$  ▷ remove all edges from node  $i$  to  $j$ 
15:      if  $\lambda_\tau^{ji} < \alpha_\tau$  then
16:         $\mathbf{E} \leftarrow \text{RemoveEdges}(\mathbf{E}, j, i)$  ▷ remove all edges from node  $j$  to  $i$ 
17:      else
18:         $\mathbf{E} \leftarrow \text{RemoveEdges}(\mathbf{E}, i, j)$  ▷ remove all edges from node  $i$  to  $j$ 
19:         $\mathbf{E} \leftarrow \text{RemoveEdges}(\mathbf{E}, j, i)$  ▷ remove all edges from node  $j$  to  $i$ 
return  $\mathbf{E}$ 
```

$\mathcal{S}_e + \Gamma_e$. However, we have observed varying CD accuracy across the l_m 's, which is attributed to the dependency of the partial correlation CI test on data size. The value of l_m affects data compression, resulting in varying data sizes and relative frequencies of 0s and 1s in the binary data. The lower $l_m = \tau_{\max} = 5$ achieves the best score, as spurious links increase for longer l_m due to higher sparsity attribution with uniform binary sequences longer than the τ_{\max} .

References

- [1] Pol, A.A., Azzolini, V., Cerminara, G., De Guio, F., Franzoni, G., Pierini, M., Sirokỳ, F., Vlimant, J.-R.: Anomaly detection using deep autoencoders for the assessment of the quality of the data acquired by the CMS experiment. In: EPJ Web of Conferences, vol. 214, p. 06008 (2019). EDP Sciences
- [2] Wielgosz, M., Mertik, M., Skoczeń, A., De Matteis, E.: The model of an anomaly detector for HiLumi LHC magnets based on

Algorithm 6 Γ_e : Pruning and adjusting time-lagged causality edges

```

1: procedure  $\Gamma_e(\mathbf{E}, \text{prune\_order} = ['t', 'w'])$ 
    $\triangleright$  Aggregates edge time lags and orients the best edges from bidirected links
    $\triangleright \mathbf{E} \in \mathbb{R}^{N \times 4}$  is a matrix of weighted directed time-lagged edge links  $\varepsilon(v, \nu, w, t)$ 
2:    $\mathbf{G}_\varepsilon \leftarrow \text{EdgeGroupMaxWeightedTimeLag}(\mathbf{E})$   $\triangleright$  groups same-nodes edges and peak the strongest time-lag
3:    $\mathbf{P} \leftarrow []$   $\triangleright$  placeholder for edges to be pruned
4:    $\mathbf{U} \leftarrow []$   $\triangleright$  placeholder for undirected edges
5:   for  $\varepsilon_s, \varepsilon_r \in \text{GetBidirectLinkedNodes}(\mathbf{G}_\varepsilon)$  : do  $\triangleright$  the current edge  $\varepsilon_s$  and the reverse edge  $\varepsilon_r$ 
6:      $\varepsilon_p \leftarrow \text{COMPAREBIDIRECTLINKS}(\varepsilon_s, \varepsilon_r, m = \text{prune\_order}[0])$   $\triangleright$  get the edge to be pruned
7:     if  $\varepsilon_p = \text{Null}$  then
8:        $\varepsilon_p \leftarrow \text{COMPAREBIDIRECTLINKS}(\varepsilon_s, \varepsilon_r, m = \text{prune\_order}[1])$   $\triangleright$  get the edge to be pruned
9:       if  $\varepsilon_p = \text{Null}$  then
10:         $\mathbf{U} \leftarrow \text{Append}(\mathbf{U}, [\varepsilon_s, \varepsilon_r])$   $\triangleright$  add the edges  $\varepsilon_s$  and  $\varepsilon_r$  into the undirected bucket
11:         $\mathbf{P} \leftarrow \text{Append}(\mathbf{P}, [\varepsilon_s, \varepsilon_r])$   $\triangleright$  add the edge  $\varepsilon_s$  and  $\varepsilon_r$  into prune bucket
12:       else
13:         $\mathbf{P} \leftarrow \text{Append}(\mathbf{P}, \varepsilon_p)$   $\triangleright$  add the edge  $\varepsilon_p$  into prune bucket
14:       else
15:         $\mathbf{P} \leftarrow \text{Append}(\mathbf{P}, \varepsilon_p)$   $\triangleright$  add the edge  $\varepsilon_p$  into prune bucket
16:    $\bar{\mathbf{E}}_R \leftarrow \text{PruneEdges}(\mathbf{G}_\varepsilon, \mathbf{P})$   $\triangleright$  remove edges in the prune bucket
17:    $\bar{\mathbf{E}}_D \leftarrow \text{DirectEdges}(\mathbf{G}_\varepsilon, \mathbf{U})$   $\triangleright$  get DAG for the undirected edges without altering the directed edges in  $\mathbf{G}_\varepsilon$ 
18:    $\bar{\mathbf{E}} \leftarrow \text{Merge}(\bar{\mathbf{E}}_R, \bar{\mathbf{E}}_D)$   $\triangleright$  merge pruned and directed edges
   return  $\bar{\mathbf{E}}$ 
19: procedure  $\text{COMPAREBIDIRECTLINKS}(\mathbf{G}_\varepsilon, \varepsilon_s, \varepsilon_r, m)$ 
    $\triangleright m = 'w'$  prune based on the values of the edges' weight
    $\triangleright m = 't'$  prune based on the values of the edges' time lag
20:    $t_s, w_s \leftarrow \text{GetEdgeAttributes}(\varepsilon_s)$   $\triangleright$  get edge link time-lag and weight of link  $s$ 
21:    $t_r, w_r \leftarrow \text{GetEdgeAttributes}(\varepsilon_r)$   $\triangleright$  get edge link time-lag and weight of the reverse link  $r$ 
22:   if  $m = 'w'$  then  $\triangleright$  use link weight values
23:     if  $w_s > w_r$  then
24:        $\varepsilon_p \leftarrow \varepsilon_r$ 
25:     else if  $w_s < w_r$  then
26:        $\varepsilon_p \leftarrow \varepsilon_s$ 
27:     else
28:        $\varepsilon_p \leftarrow \text{Null}$   $\triangleright$  indicates undirected edges
29:   else if  $m = 't'$  then  $\triangleright$  use link time-lag values (negative)
30:     if  $t_s < t_r$  then
31:        $\varepsilon_p \leftarrow \varepsilon_r$ 
32:     else if  $t_s > t_r$  then
33:        $\varepsilon_p \leftarrow \varepsilon_s$ 
34:     else
35:        $\varepsilon_p \leftarrow \text{Null}$   $\triangleright$  indicates undirected edges
   return  $\varepsilon_p$ 

```

Algorithm 7 Temporal Bayesian network model generation

```

1: procedure  $\text{BNGENERATION}(\Lambda, \mathcal{G})$ 
    $\triangleright \Lambda \in \mathcal{B}^{n \times N}$  is multivariate TS binary anomaly data
    $\triangleright \mathcal{G}$  is a graph network with  $\mathcal{G}(v, \nu, \varepsilon(w, t))$ 
2:    $\hat{\mathcal{G}} \leftarrow \text{UnrollTemporalGraph}(\mathcal{G})$   $\triangleright$  update node names with edge time-lag value, Eq. 15
    $\triangleright$  The loop below is for TS data unrolling, adopted from TPC [58]
3:    $\hat{\Lambda} \leftarrow []$   $\triangleright$  empty place holder for the unrolled TS data
4:   for  $\varepsilon(v_t, \nu) \in \text{GetLinkedNodes}(\mathcal{G})$  : do
5:      $t \leftarrow \text{GetEdgeTimeLag}(v_t)$   $\triangleright$  get source node time-lag
6:     if  $t < 0$  then  $\triangleright$  checks the time delayed causality
7:        $x_v \leftarrow \Lambda[v]$   $\triangleright$  get TS data of the  $v$  sensor,  $x_v \in \mathbb{R}^{1 \times T}$ 
8:        $\hat{x}_v \leftarrow \text{GetTimeDelayedData}(x_v, t)$   $\triangleright$  shifts backward the TS  $x_v$  by  $t$  time steps
9:        $\hat{\Lambda} \leftarrow \text{Append}(\hat{\Lambda}, \hat{x}_v)$ 
10:    $\mathcal{M}_b \leftarrow \text{FitBayesianNetwork}(\hat{\Lambda}, \hat{\mathcal{G}})$   $\triangleright$  build BN model
   return  $\mathcal{M}_b$ 

```

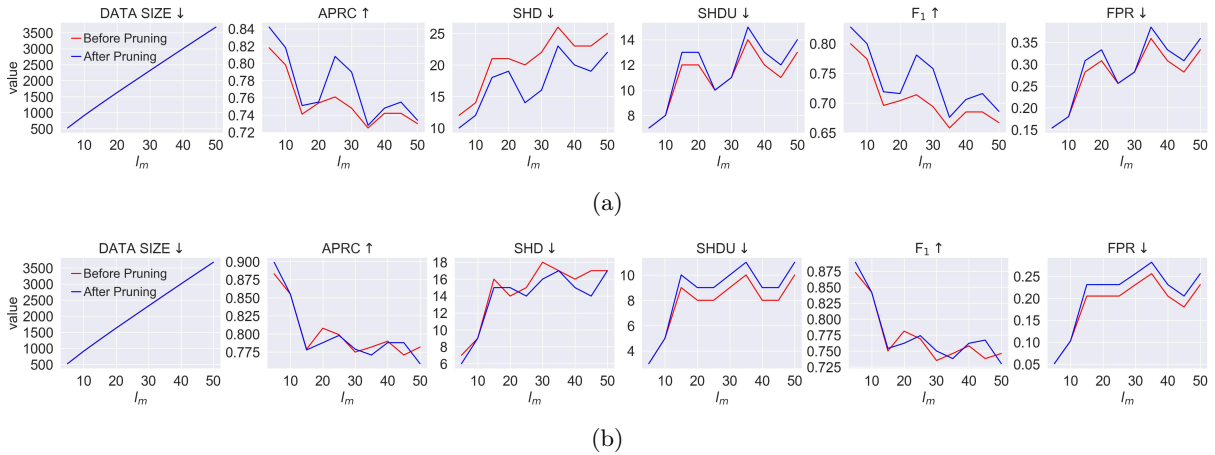


Fig. B1: Causal graph learning comparison on $\tau_{\max} = 5$ and different sparsity length $l_m = 5, 10, \dots, 50$: a) with sparse data handling, and b) with sparse data and link handling. The accuracy scores are measured with respect to the domain GCM of the HCAL given in Fig. 10.

recurrent neural networks and adaptive quantization. *Engineering Applications of Artificial Intelligence* **74**, 166–185 (2018)

- [3] Autoencoder-based anomaly detection system for online data quality monitoring of the cms electromagnetic calorimeter. *Computing and Software for Big Science* **8**(1), 11 (2024)
- [4] Asres, M.W., Cummings, G., Parygin, P., Khukhunaishvili, A., Toms, M., Campbell, A., Cooper, S.I., Yu, D., Dittmann, J., Omlin, C.W.: Unsupervised deep variational model for multivariate sensor anomaly detection. In: *International Conference on Progress in Informatics and Computing*, pp. 364–371 (2021). IEEE
- [5] Asres, M.W., Cummings, G., Khukhunaishvili, A., Parygin, P., Cooper, S.I., Yu, D., Dittmann, J., Omlin, C.W.: Long horizon anomaly prediction in multivariate time series with causal autoencoders. In: *PHM Society European Conference*, vol. 7, pp. 21–31 (2022)
- [6] Asres, M.W., Omlin, C.W., Wang, L., Yu, D., Parygin, P., Dittmann, J., Karapostoli, G., Seidel, M., Venditti, R., Lambrecht, L., *et al.*: Spatio-temporal anomaly detection with graph networks for data quality monitoring of the Hadron Calorimeter. *Sensors* **23**(24), 9679 (2023)
- [7] Asres, M.W., Omlin, C.W., Wang, L., Yu, D., Parygin, P., Dittmann, J., The CMS-HCAL Collaboration: Data quality monitoring for the Hadron Calorimeters using transfer learning for anomaly detection. *Sensors* **25**(11), 3475 (2025)
- [8] Rashidi, B., Singh, D.S., Zhao, Q.: Data-driven root-cause fault diagnosis for multivariate non-linear processes. *Control Engineering Practice* **70**, 134–147 (2018)
- [9] Leonhardt, V., Claus, F., Garth, C.: PEN: process estimator neural network for root cause analysis using graph convolution. *Journal of Manufacturing Systems* **62**, 886–902 (2022)
- [10] Ariza-Porras, C., Kuznetsov, V., Legger, F.: The CMS monitoring infrastructure and applications. *Computing and Software for Big Science* **5**(1), 5 (2021)
- [11] Gerhardus, A., Runge, J.: High-recall causal discovery for autocorrelated time series with latent confounders. *NIPS* **33**, 12615–12625 (2020)
- [12] Asres, M.W., Omlin, C.W., Dittmann, J., Parygin, P., Hiltbrand, J., Cooper, S.I., Cummings, G., Yu, D.: Lightweight multi-system multivariate interconnection and divergence discovery. In: *19th Annual System of Systems*

- Engineering Conference (SoSE), pp. 36–43 (2024). IEEE
- [13] Steenwinckel, B., De Paepe, D., Haute, S.V., Heyvaert, P., Bentefrit, M., Moens, P., Dimou, A., Van Den Bossche, B., De Turck, F., Van Hoecke, S., *et al.*: FLAGS: a methodology for adaptive anomaly detection and root cause analysis on sensor data streams by fusing expert knowledge with machine learning. *Future Generation Computer Systems* **116**, 30–48 (2021)
- [14] Martinez-Gil, J., Buchgeher, G., Gabauer, D., Freudenthaler, B., Filipiak, D., Fensel, A.: Root cause analysis in the industrial domain using knowledge graphs: a case study on power transformers. *Procedia Computer Science* **200**, 944–953 (2022)
- [15] Glymour, C., Zhang, K., Spirtes, P.: Review of causal discovery methods based on graphical models. *Frontiers in genetics* **10**, 524 (2019)
- [16] Guo, R., Cheng, L., Li, J., Hahn, P.R., Liu, H.: A survey of learning causality with data: problems and methods. *ACM Computing Surveys* **53**(4), 1–37 (2020)
- [17] Liu, C., Lore, K.G., Jiang, Z., Sarkar, S.: Root-cause analysis for time-series anomalies via spatiotemporal graphical modeling in distributed complex systems. *Knowledge-Based Systems* **211**, 106527 (2021)
- [18] Böhmer, K., Rinderle-Ma, S.: Mining association rules for anomaly detection in dynamic process runtime behavior and explaining the root cause to users. *Information Systems* **90**, 101438 (2020)
- [19] Tian, C., Zhao, C., Fan, H., Zhang, Z.: Causal network construction based on convergent cross mapping (CCM) for alarm system root cause tracing of nonlinear industrial process. *IFAC-PapersOnLine* **53**(2), 13619–13624 (2020)
- [20] Nauta, M., Bucur, D., Seifert, C.: Causal discovery with attention-based convolutional neural networks. *Machine Learning and Knowledge Extraction* **1**(1), 312–340 (2019)
- [21] Zhou, Y., Xu, K., He, F.: Root cause diagnosis in multivariate time series based on modified temporal convolution and multi-head self-attention. *Journal of Process Control* **117**, 14–25 (2022)
- [22] Wang, P., Xu, J., Ma, M., Lin, W., Pan, D., Wang, Y., Chen, P.: CloudRanger: root cause identification for cloud native systems. In: *18th International Symposium on Cluster, Cloud and Grid Computing*, pp. 492–502 (2018). IEEE
- [23] Budhathoki, K., Janzing, D., Bloebaum, P., Ng, H.: Why did the distribution change? In: *International Conference on Artificial Intelligence and Statistics*, pp. 1666–1674 (2021). PMLR
- [24] Budhathoki, K., Minorics, L., Blöbaum, P., Janzing, D.: Causal structure-based root cause analysis of outliers. In: *ICML*, pp. 2357–2369 (2022). PMLR
- [25] Assaad, C.K., Ez-Zejjari, I., Zan, L.: Root cause identification for collective anomalies in time series given an acyclic summary causal graph with loops. In: *International Conference on Artificial Intelligence and Statistics*, pp. 8395–8404 (2023). PMLR
- [26] Runge, J.: Causal network reconstruction from time series: from theoretical assumptions to practical estimation. *Chaos: an Interdisciplinary Journal of Nonlinear Science* **28**(7) (2018)
- [27] Runge, J.: Discovering contemporaneous and lagged causal relations in autocorrelated nonlinear time series datasets. In: *Conference on Uncertainty in Artificial Intelligence*, pp. 1388–1397 (2020). PMLR
- [28] Runge, J., Nowack, P., Kretschmer, M., Flaxman, S., Sejdinovic, D.: Detecting and quantifying causal associations in large nonlinear time series datasets. *Science Advances* **5**(11), 4996 (2019)
- [29] Saggioro, E., Wiljes, J., Kretschmer, M.,

- Runge, J.: Reconstructing regime-dependent causal relationships from observational time series. *Chaos: an Interdisciplinary Journal of Nonlinear Science* **30**(11) (2020)
- [30] Niu, W., Gao, Z., Song, L., Li, L.: Comprehensive review and empirical evaluation of causal discovery algorithms for numerical data. arXiv preprint arXiv:2407.13054 (2024)
- [31] Kalisch, M., Bühlman, P.: Estimating high-dimensional directed acyclic graphs with the PC-algorithm. *JMLR* **8**(3) (2007)
- [32] Li, J., Wang, Z.J.: Controlling the false discovery rate of the association/causality structure learned with the pc algorithm. *JMLR* **10**(2) (2009)
- [33] Amornbunchornvej, C., Surasvadi, N., Plangprasopchok, A., Thajchayapong, S.: Framework for inferring empirical causal graphs from binary data to support multidimensional poverty analysis. *Heliyon* **9**(5) (2023)
- [34] Neapolitan, R.E., *et al.*: *Learning Bayesian Networks* vol. 38. Pearson Prentice Hall, United States (2004)
- [35] Meng, Y., Zhang, S., Sun, Y., Zhang, R., Hu, Z., Zhang, Y., Jia, C., Wang, Z., Pei, D.: Localizing failure root causes in a microservice through causality inference. In: 28th International Symposium on Quality of Service, pp. 1–10 (2020). IEEE
- [36] Spirtes, P., Glymour, C.N., Scheines, R.: *Causation, Prediction, and Search*. MIT press, United States (2000)
- [37] Chevalley, M., Roohani, Y., Mehrjou, A., Leskovec, J., Schwab, P.: CausalBench: a large-scale benchmark for network inference from single-cell perturbation data. arXiv preprint arXiv:2210.17283 (2022)
- [38] Chen, J., Zhao, C.: Multi-lag and multi-type temporal causality inference and analysis for industrial process fault diagnosis. *Control Engineering Practice* **124**, 105174 (2022)
- [39] Chen, Q., Lang, X., Lu, S., Rehman, N., Xie, L., Su, H.: Detection and root cause analysis of multiple plant-wide oscillations using multivariate nonlinear chirp mode decomposition and multivariate Granger causality. *Computers and Chemical Engineering* **147**, 107231 (2021)
- [40] Qin, K., Chen, L., Shi, J., Li, Z., Hao, K.: Root cause analysis of industrial faults based on binary extreme gradient boosting and temporal causal discovery network. *Chemometrics and Intelligent Laboratory Systems* **225**, 104559 (2022)
- [41] Liu, N., Hu, M., Wang, J., Ren, Y., Tian, W.: Fault detection and diagnosis using bayesian network model combining mechanism correlation analysis and process data: application to unmonitored root cause variables type faults. *Process Safety and Environmental Protection* **164**, 15–29 (2022)
- [42] De Paepe, D., Hautte, S.V., Steenwinckel, B., De Turck, F., Ongenae, F., Janssens, O., Van Hoecke, S.: A generalized matrix profile framework with support for contextual series analysis. *Engineering Applications of Artificial Intelligence* **90**, 103487 (2020)
- [43] Lundberg, S.M., Lee, S.-I.: A unified approach to interpreting model predictions. *NIPS* **30** (2017)
- [44] Margaritis, D., *et al.*: *Learning bayesian network model structure from data*. PhD thesis, School of Computer Science, Carnegie Mellon University Pittsburgh, PA, USA (2003)
- [45] Tsamardinos, I., Aliferis, C.F., Statnikov, A.R., Statnikov, E.: Algorithms for large scale Markov blanket discovery. In: *FLAIRS Conference*, vol. 2, pp. 376–380 (2003). St. Augustine, FL
- [46] Tsamardinos, I., Aliferis, C.F., Statnikov, A.: Time and sample efficient discovery of Markov blankets and direct causal relations. In: *Proceedings of the 9th ACM SIGKDD*, pp. 673–678 (2003)

- [47] Colombo, D., Maathuis, M.H., *et al.*: Order-independent constraint-based causal structure learning. *JMLR* **15**(1), 3741–3782 (2014)
- [48] Tsamardinos, I., Brown, L.E., Aliferis, C.F.: The max-min hill-climbing Bayesian network structure learning algorithm. *Machine Learning* **65**, 31–78 (2006)
- [49] Koller, D., Friedman, N.: *Probabilistic Graphical Models: Principles and Techniques*. MIT press, United States (2009)
- [50] Chickering, D.M.: Optimal structure identification with greedy search. *JMLR* **3**, 507–554 (2002)
- [51] Ramsey, J.D.: Scaling up greedy causal search for continuous variables. *arXiv preprint arXiv:1507.07749* (2015)
- [52] Ogarrio, J.M., Spirtes, P., Ramsey, J.: A hybrid causal search algorithm for latent variable models. In: *Conference on Probabilistic Graphical Models*, pp. 368–379 (2016). PMLR
- [53] Bühlmann, P., Peters, J., Ernest, J.: CAM: causal additive models, high-dimensional order search and penalized regression. *The Annals of Statistics* **42**, 2526–2556 (2014)
- [54] Goudet, O., Kalainathan, D., Caillou, P., Guyon, I., Lopez-Paz, D., Sebag, M.: Learning functional causal models with generative neural networks. *Explainable and Interpretable Models in Computer Vision and Machine Learning*, 39–80 (2018)
- [55] Peters, J., Janzing, D., Schölkopf, B.: *Elements of Causal Inference: Foundations and Learning Algorithms*. The MIT Press, United States (2017)
- [56] Liu, Y., Chen, H.-S., Wu, H., Dai, Y., Yao, Y., Yan, Z.: Simplified granger causality map for data-driven root cause diagnosis of process disturbances. *Journal of Process Control* **95**, 45–54 (2020)
- [57] Shojaie, A., Fox, E.B.: Granger causality: a review and recent advances. *Annual Review of Statistics and Its Application* **9**, 289–319 (2022)
- [58] Biswas, R., Shlizerman, E.: Statistical perspective on functional and causal neural connectomics: the time-aware pc algorithm. *PLOS Computational Biology* **18**(11), 1010653 (2022)
- [59] The CMS Collaboration, Chatrchyan, S., Hmayakyan, G., Khachatryan, V., Sirunyan, A., Adam, W., Bauer, T., Bergauer, T., Bergauer, H., Dragicevic, M., *et al.*: The CMS experiment at the CERN LHC. *Journal of Instrumentation* **3**, 08004 (2008)
- [60] Hayrapetyan, A., *et al.*: Development of the CMS detector for the CERN LHC Run 3. *JINST* **19**(05), 05064 (2024) <https://doi.org/10.1088/1748-0221/19/05/P05064>
- [61] Strobbe, N.: The upgrade of the CMS Hadron Calorimeter with Silicon photomultipliers. *Journal of Instrumentation* **12**(1), 01080 (2017)
- [62] Focardi, E.: Status of the CMS detector. *Physics Procedia* **37**, 119–127 (2012)
- [63] Mans, J.: CMS technical design report for the phase 1 upgrade of the hadron calorimeter. Technical report, CMS-TDR-010 (2012)
- [64] Baiatian, G., Hashemi, M., Hagopian, S., Pal, A., Machado, E., Isiksal, E., Odell, V., Haelen, T., Sanders, D.A., Yazgan, E., *et al.*: Design, performance, and calibration of CMS Hadron Endcap calorimeters. Technical report, CERN-CMS-NOTE-2008-010 (2008)
- [65] EasyVista. <https://www.easyvista.com/fr/produits/ev-observe>. Accessed: 2023-01-10
- [66] EasyRCA IT monitoring dataset. <https://github.com/ckassaad/EasyRCA>. Accessed: 2023-01-10
- [67] Karim, F., Majumdar, S., Darabi, H., Harford, S.: Multivariate LSTM-FCNs for time series classification. *Neural Networks* **116**, 237–245 (2019)

- [68] Cleveland, R.B., Cleveland, W.S., McRae, J.E., Terpenning, I.: STL: a seasonal-trend decomposition. *J. Off. Stat* **6**(1), 3–73 (1990)
- [69] Bandara, K., Hyndman, R.J., Bergmeir, C.: MSTL: a seasonal-trend decomposition algorithm for time series with multiple seasonal patterns. *arXiv preprint arXiv:2107.13462* (2021)
- [70] Ren, H., Xu, B., Wang, Y., Yi, C., Huang, C., Kou, X., Xing, T., Yang, M., Tong, J., Zhang, Q.: Time-series anomaly detection service at Microsoft. In: *Proceedings of the 25th ACM SIGKDD*, pp. 3009–3017 (2019)
- [71] Castri, L., Mghames, S., Hanheide, M., Bellotto, N.: Enhancing causal discovery from robot sensor data in dynamic scenarios. In: *Conference on Causal Learning and Reasoning*, pp. 243–258 (2023). PMLR
- [72] Tárraga, J.M., Sevillano-Marco, E., Muñoz-Marí, J., Piles, M., Sitokonstantinou, V., Ronco, M., Miranda, M.T., Cerdà, J., Camps-Valls, G.: Causal discovery reveals complex patterns of drought-induced displacement. *IScience* **27**(9) (2024)
- [73] Bishop, Y.M., Fienberg, S.E., Holland, P.W.: *Discrete Multivariate Analysis: Theory and Practice*. Springer, United States (2007)
- [74] Murphy, K.P.: *Dynamic Bayesian Networks: Representation, Inference and Learning*. University of California, Berkeley, United States (2002)
- [75] Sheidaei, A., Foroushani, A.R., Gohari, K., Zeraati, H.: A novel dynamic Bayesian network approach for data mining and survival data analysis. *BMC Medical Informatics and Decision Making* **22**(1), 1–15 (2022)
- [76] Peters, J., Bühlmann, P.: Structural intervention distance for evaluating causal graphs. *Neural Computation* **27**(3), 771–799 (2015)
- [77] Zhang, K., Zhu, S., Kalander, M., Ng, I., Ye, J., Chen, Z., Pan, L.: gcastle: a python toolbox for causal discovery. *arXiv preprint arXiv:2111.15155* (2021)
- [78] Carvalho, A.M.: Scoring functions for learning bayesian networks. *Inesc-id Tec. Rep* **12**, 1–48 (2009)
- [79] Shimizu, S., Inazumi, T., Sogawa, Y., Hyvärinen, A., Kawahara, Y., Washio, T., Hoyer, P.O., Bollen, K., Hoyer, P.: DirectLiNGAM: a direct method for learning a linear non-Gaussian structural equation model. *JMLR* **12**(Apr), 1225–1248 (2011)
- [80] Shimizu, S., Hoyer, P.O., Hyvärinen, A., Kerminen, A., Jordan, M.: A linear non-Gaussian acyclic model for causal discovery. *JMLR* **7**(10) (2006)
- [81] Lachapelle, S., Brouillard, P., Deleu, T., Lacoste-Julien, S.: Gradient-based neural dag learning. *arXiv preprint arXiv:1906.02226* (2019)
- [82] Ng, I., Ghassami, A., Zhang, K.: On the role of sparsity and dag constraints for learning linear dags. *NIPS* **33**, 17943–17954 (2020)
- [83] Ng, I., Zhu, S., Chen, Z., Fang, Z.: A graph autoencoder approach to causal structure learning. *arXiv preprint arXiv:1911.07420* (2019)
- [84] Zhu, S., Ng, I., Chen, Z.: Causal discovery with reinforcement learning. *arXiv preprint arXiv:1906.04477* (2019)
- [85] Wang, X., Du, Y., Zhu, S., Ke, L., Chen, Z., Hao, J., Wang, J.: Ordering-based causal discovery with reinforcement learning. *arXiv preprint arXiv:2105.06631* (2021)

The CMS-HCAL Collaboration

M.W. Asres¹, C.W. Omlin¹, V. Chekhovskiy^{2,a}, A. Chinaryan², A. Gevorgyan², Ya. Halkin², A. Kunts², A. Litomin^{2,a}, A. Petrosyan², A. Tumasyan², H. Saka³, A. Stepennov³, G. Karapostoli⁴, A. Campbell⁵, F. Engelke⁵, M. Csanád⁶, A. Feherkuti^{6,b}, G. Pásztor⁶, G.I. Veres⁶, S. Bhattacharya⁷, M.M. Ameen^{8,c}, M. Guchait⁸, G. Majumder⁸, K. Mazumdar^{8,d}, M. Patil⁸, A. Thachayath⁸, T. Mishra^{9,e}, P. Sadangi⁹, H. Hwang¹⁰, J. Padmanaban¹⁰, J. Yoo¹⁰, D. Agyel¹¹, Z. Azimi¹¹, I. Dumanoglu^{11,f}, E. Eskut¹¹, Y. Guler^{11,g}, E. Gurpinar Guler^{11,g}, C. Isik¹¹, O. Kara¹¹, A. Kayis Topaksu¹¹, G. Onengut^{11,d}, K. Ozdemir^{11,h}, A. Polatoz¹¹, B. Tali^{11,i}, U.G. Tok¹¹, E. Uslan¹¹, I.S. Zorbakir¹¹, B. Akgun¹², I.O. Atakisi¹², B. Gonultas¹², E. Gülmez¹², M. Kaya^{12,j}, O. Kaya^{12,k}, S. Tekten^{12,l}, E.A. Yetkin^{12,m}, B. Balci¹³, K. Cankocak^{13,f}, G.G. Dincer¹³, Y. Komurcu¹³, I. Ozsahin¹³, S. Sen^{13,n}, S. Cerci¹⁴, A.A. Guvenli¹⁴, E. Iren^{14,o}, B. Isildak¹⁴, O.B. Kolcu^{14,p}, E. Simsek^{14,q}, D. Sunar Cerci¹⁴, T. Yetkin^{14,p}, B. Haciasahinoglu¹⁵, I. Hos^{15,r}, B. Kaynak¹⁵, S. Ozkorucuklu¹⁵, O. Potok¹⁵, H. Sert¹⁵, C. Simsek¹⁵, C. Zorbilmez¹⁵, L. Levchuk¹⁶, V. Popov¹⁶, S. Abdullin¹⁷, H. Buttrum¹⁷, J. Dittmann¹⁷, T. Efthymiadou¹⁷, K. Hatakeyama¹⁷, J. Hiltbrand¹⁷, A. Kalinin^{17,a}, J. Wilson¹⁷, P. Bunin^{18,a}, S.I. Cooper¹⁸, C. Crovella¹⁸, E. Pearson¹⁸, C.U. Perez^{18,s}, P. Rumerio^{18,t}, R. Yi¹⁸, C. Cosby¹⁹, Z. Demiragli¹⁹, D. Gastler¹⁹, E. Hazen¹⁹, J. Rohlf¹⁹, E. Wurtz¹⁹, M. Hadley²⁰, T. Kwon²⁰, G. Landsberg²⁰, K.T. Lau²⁰, M. Stamenkovic²⁰, X. Yan^{20,u}, D.R. Yu^{20,v}, A. Apresyan²¹, S. Banerjee^{21,w}, F. Chlebana²¹, G. Cummings²¹, Y. Feng^{21,x}, J. Freeman²¹, D. Green^{21,d}, J. Hirschauer²¹, U. Joshi²¹, K.H.M. Kwok²¹, D. Lincoln²¹, S. Los²¹, C. Madrid^{21,x}, N. Pastika²¹, K. Pedro²¹, S. Tkaczyk²¹, V. Hagopian^{22,†}, T. Kolberg²², G. Martinez²², M. Alhousseini²³, B. Bilki^{23,y}, D. Blend²³, P. Debbins²³, K. Dilsiz^{23,z}, L. Emediato²³, F.D. Ingram²³, O.K. Köseyan²³, J.-P. Merlo²³, A. Mestvirishvili^{23,aa}, M. Miller²³, H. Ogul^{23,bb}, Y. Onel²³, A. Penzo²³, I. Schmidt²³, D. Southwick²³, E. Tiras^{23,cc}, J. Wetzel²³, L.F. Alcerro Alcerro²⁴, S. Arteaga Escatel²⁴, J. Bowen^{24,dd}, M.R. Chukwuka²⁴, C. Le Mahieu²⁴, J. Marquez²⁴, J. Mbagwu²⁴, M. Murray²⁴, M. Nickel²⁴, S. Popescu²⁴, C. Smith²⁴, N. Islam²⁵, K. Kaadze²⁵, D. Kim²⁵, Y. Maravin²⁵, J. Natoli²⁵, D. Roy²⁵, R.D. Taylor²⁵, A. Baden²⁶, A. Belloni²⁶, J. Bistany-riebman²⁶, A. Bussio²⁶, Y.M. Chen²⁶, S.C. Eno²⁶, T. Grassi²⁶, N.J. Hadley^{26,d}, R.G. Kellogg^{26,d}, T. Koeth²⁶, B. Kronheim²⁶, Y. Lai²⁶, S. Lascio²⁶, A.C. Mignerey²⁶, S. Nabili²⁶, C. Palmer²⁶, C. Papageorgakis²⁶, M.M. Paranjpe²⁶, E. Popova^{26,a}, M. Seidel^{26,ee}, A. Skuja²⁶, L. Wang²⁶, H. Bossi²⁷, M. D'Alfonso²⁷, G.M. Innocenti²⁷, M. Klute²⁷, J. Krupa²⁷, M. Hu²⁷, J. Lang²⁷, C. McGinn²⁷, B. Crossman²⁸, C. Kapsiak²⁸, M. Krohn²⁸, J. Mans²⁸, M. Revering²⁸, N. Strobbe²⁸, A. Das²⁹, A. Heering²⁹, N. Loukas²⁹, J. Mariano²⁹, Y. Musienko^{29,a}, R. Ruchti²⁹, M. Wayne²⁹, A.D. Benaglia³⁰, W. Chung³⁰, S. Hoienko³⁰, K. Kennedy³⁰, G. Kopp³⁰, T. Medvedeva³⁰, K. Mei³⁰, C. Tully³⁰, O. Bessidskaia Bylund³¹, A. Bodek³¹, P. de Barbaro³¹, A. Garcia-Bellido³¹, A. Khukhunaishvili³¹, N. Parmar³¹, P. Parygin^{31,a}, C.L. Tan³¹, R. Taus³¹, B. Chiarito³², J.P. Chou³², S.A. Thayil³², H. Wang³², N. Akchurin³³, N. Gogate³³, J. Damgov³³, S. Kunori³³, K. Lamichhane³³, S.W. Lee³³, S. Magedov³³, A. Menkel³³, S. Undleeb³³, I. Volobouev³³, H. Chung³⁴, S. Goadhouse³⁴, J. Hakala³⁴, R. Hirosky³⁴, V. Alexakhin³⁵, V. Andreev³⁵, Yu. Andreev³⁵, T. Aushev³⁵, M. Azarkin³⁵, A. Belyaev³⁵, S. Bitioukov^{35,†}, E. Boos³⁵, K. Bukin³⁵, O. Bychkova³⁵, M. Chadeeva^{35,a}, R. Chistov^{35,a}, M. Danilov^{35,a}, A. Demianov³⁵, A. Dermenev³⁵, M. Dubinin^{35,ff}, L. Dudko³⁵, D. Elumakhov³⁵, Y. Ershov³⁵, A. Ershov³⁵, V. Gavrilov³⁵, I. Golutvin^{35,†}, N. Gorbunov³⁵, A. Gribushin^{35,a}, A. Kaminskiy³⁵, V. Karjavine³⁵, A. Karneyev³⁵, L. Khein³⁵, M. Kirakosyan³⁵, V. Klyukhin^{35,a}, O. Kodolova^{35,gg}, N. Krasnikov³⁵, V. Krychkin^{35,†}, A. Kurenkov³⁵, N. Lychkovskaya³⁵, V. Makarenko^{35,gg}, P. Mandrik³⁵, P. Moisez^{35,†}, V. Mossolov^{35,gg}, S. Obraztsov³⁵, A. Oskin³⁵, V. Petrov³⁵, S. Petrushanko^{35,a}, S. Polikarpov^{35,a}, V. Rusinov³⁵, R. Ryutin³⁵, V. Savrin³⁵, D. Selivanova³⁵, V. Smirnov³⁵, A. Snigirev³⁵, A. Sobol³⁵, E. Tarkovskii³⁵, A. Terkulov³⁵, D. Tlisov^{35,†}, I. Tlisova³⁵, R. Tolochek³⁵, M. Toms^{35,hh}, A. Toropin³⁵, S. Troshin³⁵, A. Volkov³⁵, P. Volkov³⁵, B. Yuldashev^{35,†}, A. Zarubin³⁵, A. Zhokin³⁵

- ¹University of Agder, Grimstad, Norway*
- ²Yerevan Physics Institute, Yerevan, Armenia
- ³Department of Physics, University of Cyprus, Nicosia, Cyprus
- ⁴National Technical University of Athens, Athens, Greece
- ⁵Deutsches Elektronen-Synchrotron, Hamburg, Germany*
- ⁶MTA-ELTE Lendület CMS Particle and Nuclear Physics Group, Eötvös Loránd University, Budapest, Hungary
- ⁷Saha Institute of Nuclear Physics, Kolkata, India*
- ⁸Tata Institute of Fundamental Research-B, Mumbai, India
- ⁹National Institute of Science Education and Research, Odisha, India*
- ¹⁰Korea University, Seoul, Korea
- ¹¹Çukurova University, Physics Department, Science and Art Faculty, Adana, Turkey
- ¹²Bogazici University, Istanbul, Turkey
- ¹³Istanbul Technical University, Istanbul, Turkey
- ¹⁴Yildiz Technical University, Istanbul, Turkey
- ¹⁵Istanbul University, Istanbul, Turkey
- ¹⁶National Science Centre, Kharkiv Institute of Physics and Technology, Kharkiv, Ukraine
- ¹⁷Baylor University, Waco, Texas, USA
- ¹⁸The University of Alabama, Tuscaloosa, Alabama, USA
- ¹⁹Boston University, Boston, Massachusetts, USA
- ²⁰Brown University, Providence, Rhode Island, USA
- ²¹Fermi National Accelerator Laboratory, Batavia, Illinois, USA
- ²²Florida State University, Tallahassee, Florida, USA
- ²³The University of Iowa, Iowa City, Iowa, USA
- ²⁴The University of Kansas, Lawrence, Kansas, USA
- ²⁵Kansas State University, Manhattan, Kansas, USA
- ²⁶University of Maryland, College Park, Maryland, USA
- ²⁷Massachusetts Institute of Technology, Cambridge, Massachusetts, USA
- ²⁸University of Minnesota, Minneapolis, Minnesota, USA
- ²⁹University of Notre Dame, Notre Dame, Indiana, USA
- ³⁰Princeton University, Princeton, New Jersey, USA
- ³¹University of Rochester, Rochester, New York, USA
- ³²Rutgers, The State University of New Jersey, Piscataway, New Jersey, USA
- ³³Texas Tech University, Lubbock, Texas, USA
- ³⁴University of Virginia, Charlottesville, Virginia, USA
- ³⁵Authors affiliated with an institute or an international laboratory covered by a cooperation agreement with CERN

*No longer in CMS HCAL Collaboration

†: Deceased

^aAlso at an institute or an international laboratory covered by a cooperation agreement with CERN

^bAlso at HUN-REN Wigner Research Centre for Physics, Budapest, Hungary

^cNow at Indian Institute of Technology Madras, Chennai, India

^dEmeritus

^eNow at Indian Institute of Science, Bangalore, India

^fAlso at Near East University, Research Center of Experimental Health Science, Nicosia, Turkey

^gAlso at Konya Technical University, Konya, Turkey

^hAlso at Bakircay University, Izmir, Turkey

ⁱAlso at Adiyaman University, Adiyaman, Turkey

^jAlso at Marmara University, Istanbul, Turkey

^kAlso at Milli Savunma University, Istanbul, Turkey
^lAlso at Kafkas University, Kars, Turkey
^mAlso at Istanbul Bilgi University, Istanbul, Turkey
ⁿAlso at Hacettepe University, Ankara, Turkey
^oAlso at Mimar Sinan Fine Arts University, Istanbul, Turkey
^pAlso at Istinye University, Istanbul, Turkey
^qAlso at Bogazici University, Istanbul, Turkey
^rAlso at Istanbul University–Cerrahpasa, Faculty of Engineering, Istanbul, Turkey
^sNow at Universitat Ramon Llull, Barcelona, Spain
^tAlso at Università di Torino, Torino, Italy
^uNow at University of California, Santa Barbara, USA
^vNow at State University of New York, Buffalo, USA
^wNow at University of Wisconsin-Madison, Madison, USA
^xNow at Texas Tech University, Lubbock, USA
^yAlso at Beykent University, Istanbul, Turkey
^zAlso at Bingol University, Bingol, Turkey
^{aa}Also at Georgian Technical University, Tbilisi, Georgia
^{bb}Also at Sinop University, Sinop, Turkey
^{cc}Also at Erciyes University, Kayseri, Turkey
^{dd}Now at Baker University, Baldwin City, USA
^{ee}Now at Riga Technical University, Riga, Latvia
^{ff}Also at California Institute of Technology, Pasadena, California, USA
^{gg}Now at Yerevan Physics Institute, Yerevan, Armenia
^{hh}Now at Karlsruhe Institute of Technology, Karlsruhe, Germany